Assessment of Impact Damage in Fully Adhered Commercial Roofing System

Assessment of Impact Damage in Fully Adhered Commercial Roofing System

by

Yi Ding

A Dissertation

Presented to the Graduate and Research Committee

of Lehigh University

in Candidacy for the Degree of

Doctor of Philosophy

in

Mechanical Engineering

Lehigh University

January 2026

Approved and recommended for acceptance as a dissertation in partial fulfillment of the requirements for the degree of Doctor of Philosophy

Yi Ding

Numerical and Experimental Investigation of Impact Damage in Fully Adhered Commercial Roofing Systems

April 28, 2025

Defense Date

Herman F. Nied

Dissertation Director

Approved Date

Committee Members:

Herman F. Nied

D. Gary Harlow

Edmund Webb III

Ray Pearson

ACKNOWLEDGMENTS

First and foremost, I would like to express my sincere gratitude to my advisor, Professor Herman F. Nied. He has been not only a teacher and mentor, but also a role model who shaped my approach to research and professional conduct. His guidance has helped me develop the mindset and discipline as a researcher, and his dedication and integrity have left a lasting impression on me, both as a student and as a person.

I would also like to sincerely thank my committee members—Professor D. Gary Harlow, Professor Edmund Webb III, and Professor Ray Pearson—for their invaluable support throughout this journey. The knowledge you have shared will remain with me for life, and the example you set through your professionalism and commitment will continue to guide me in the years ahead.

My appreciation also extends to all the faculty and staff of Department of Mechanical Engineering & Mechanics who have supported my studies. I am especially grateful for the thoughtful and sustained support provided by them, along with our university, during the COVID-19 pandemic. The flexibility and resources made available during that time helped me endure an exceptionally challenging period and mitigate the disruption to my studies.

During the course of this research, I gratefully acknowledge the generous support and assistance of GAF, as well as the dedicated technicians and staff at Packard Laboratory and the ATLSS Center. This project could not have been completed without your contributions.

I am also immensely grateful to my parents for their understanding and unwavering support in my decision to pursue further studies. Special thanks go to my wife and children, whose presence throughout this journey, have given me the strength and motivation to keep moving forward each day.

To everyone I've met along this journey — thank you. I am deeply grateful for your presence in my life, and I sincerely hope our paths will cross again.

TABLE OF CONTENTS

LIST OF TABLES

LIST OF FIGURES

ABSTRACT

A commercial Thermoplastic Polyolefin (TPO) roofing systems is a type of single-ply roofing assembly that possesses a TPO membrane as the roof cap material. The system has gained its popularity, especially in the U.S. market, for its flexibility, durability, energy efficiency, etc., Since it was introduced in the 1990s, the roofing industry has been continuously improving its performance. One key aspect is the ability to withstand surface impact conditions, such as severe hail events.

Since TPO roofing systems are typically constructed in a bottom-up, layer-by-layer manner, ultimately forming a multi-layered assembly, and each individual component within the system often consists of its own layered structure, it is understandable that the damage in any given layer during an impact event depends on the damage evolution in adjacent layers. This study investigates the response and damage characteristics of a representative commercial TPO roofing system subjected to impact loading, using a combination of experimental testing and finite element simulation. It was observed that the gypsum core of the cover board experienced severe internal fracture damage, which was shown to be closely correlated with the maximum shear stresses defined by a conical damage zone. By comparing experimental observations to the simulation results, the mechanisms behind damage initiation at other locations were also carefully examined and discussed.

Chapter 1

Introduction

1.1 TPO Commercial Roofing System

Commercial roofing systems are commonly employed in large-scale facilities such as shopping malls, office buildings, warehouses, and stadiums. These structures typically require expansive roof areas with flat or low-slope profiles to fulfill functional needs and support rooftop equipment installations. Although both commercial and residential roofs serve the fundamental purpose of providing shelter, commercial roofing systems are subject to more stringent performance expectations. They must deliver higher levels of weather resistance, improved energy efficiency, and facilitate convenient access for inspection, maintenance, and repair. These elevated requirements arise from the substantial size and operational complexity inherent to commercial buildings.

Commercial roofing systems can generally be classified into six main categories: single-ply membrane roofing, built-up roofing, modified bitumen roofing, metal roofing, spray polyurethane foam (SPF) roofing, and green roofing systems [1]. Among these, single-ply membrane roofing dominates the US market, accounting for approximately 29.4% of the regional market valued at USD 11.9 billion in 2023, and is expected to grow at a compound annual growth rate (CAGR) of 6.4% over the next several years [2] [3]. This type of roofing system is favored due to its ease of installation, high energy efficiency, long-term durability, and cost-effectiveness over the entire life cycle.

(a) Single-ply membrane [4]; (b) Build-up [5];
(c) Metal [6]; (d) Spray polyurethane foam [7].

Figure 1 Commercial Roofing Systems

Single-ply membrane roofing systems are commonly categorized according to the type of membrane material utilized, including Thermoplastic Polyolefin (TPO), Polyvinyl Chloride (PVC), Ethylene Propylene Diene Monomer (EPDM), among others. These membrane types vary in chemical composition, reflectivity, durability, and weather resistance, enabling customized performance based on specific environmental and structural demands. Among them, the TPO roofing system—used hereafter to refer to commercial roofing systems employing TPO membranes—currently dominates the market [8] and is projected to maintain steady growth in the foreseeable future. This continued expansion is driven not only by the advantageous material properties of TPO—such as high solar reflectivity, excellent resistance to ultraviolet radiation and chemical exposure, superior heat-weldability, and recyclability—but also by the system's overall durability and performance. Additionally, TPO roofing systems are well-regarded for their cost-efficiency, ease of installation, and minimal maintenance requirements, making them a preferred solution in contemporary commercial roofing practices.

The first known application of TPO membrane as a roof cap happened in Michigan, 1986. As of 2018 in the United States, TPO held a dominant share of the roofing membrane market, accounting for over 50% of installations and covering approximately 2 billion square feet annually [9].

The structural base of a TPO roofing system is typically referred to as the roof deck, which is most commonly made of steel or concrete. Above the deck, additional layers are incorporated depending on specific project requirements. These layers, arranged from bottom to top, may include a thermal barrier, a vapor retarder, one or more layers of insulation, one or more layers of cover board, and finally, the TPO membrane.

While the insulation layers are usually fastened to the roof deck using mechanical fasteners such as bolts and washer plates, the cover board and TPO membrane can be installed using one of two primary methods:

- Fully adhered: Adhesives are applied in-between the layers to bond the system components;
- Mechanically attached: Fasteners are driven through all layers and secured with washer plates (also called seam plates).

Mechanically attached systems are popular due to their lower material costs and faster, simplified installation. But fully adhered systems offer certain benefits, especially when facing the threat of hail impact. Field records of actual damage of TPO roofing systems showed that the main cause of TPO to fracture was because of hits that landed directly on top of a washer plate. At locations where field impacts happen, however, through opening on the TPO membranes was seldom seen. With that said, the fully adhere system does come with a higher cost. The fully bonded layers also have to be replaced in massive scales when damage happens. Another aspect that largely affects the performance, whether mechanically fastened or fully adhered, is the installation quality. Researches had shown plenty of evidence that improper installation can cause the system to underperform. For such a large-scale system to function as expected, anything in the loop should be carefully considered. (Ref needed).

This research focuses on a fully adhered TPO roofing system of a certain configuration. A detailed description of the system configuration will be provided in the following chapter.

Figure 2 Commercial TPO application: Saputo Cheese USA Facility in Caledonia, Wisconsin

[10]

1.2 Hail Threat to Commercial Roofing Systems

Since 2010, hailstorms that carry hailstones of a 1-in-diameter or larger are categorized as severe hail events [11]. With data [12] recorded in the Storm Prediction Center (SPC) of National Oceanic and Atmospheric Administration (NOAA), the United States experienced 7588 severe hail events annually between 2010 and 2024.

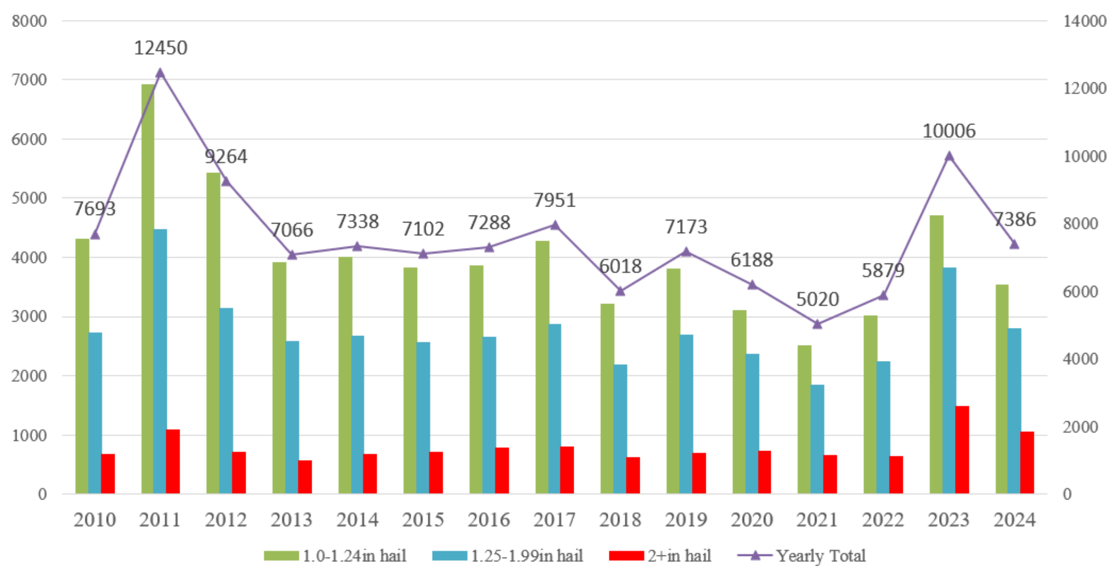

Figure 3 Number of annual sever hail events 2010~2024

The record for the largest number of severe hail events in a single year was set in 2011, when 12,450 severe-hail events were recorded. That year also holds the largest single-year counts of hail events in several sub-categories in terms of the hailstone size: 6,907 reports of 1.00–1.24 in, 4,464 reports of 1.25–1.99 in, and 1,079 reports exceeding 2.00 in, until in 2023, the second-highest year on record, 10,006 severe-hail events were reported, of which 1,477 involved hailstones 2.00 in or larger. In 2024, the total number of severe hail evens dropped back to 7386, with only 5% more of the annual average excluding 2011 and 2023. However, 1059 2+in hail events—a value comparable to 2011—were reported.

In terms of monthly occurrence, March marks the start of the hail season, with an average of 584 reported events over the past 15 years. That number is roughly doubled in April to 1189 events and peaks in May with 1861. Number of events decline from June through August. That six-month window accounts for 91% of the year's severe hail events reported on average.

Table 1 Average monthly severe hail events during 2010~2024

Month	Number of severe hail events	Largest number of severe hail events
Jan	49	144 2010
Feb	104	411 2017
Mar	584	1552 2012
Apr	1189	1745 2023
May	1861	2929 2011
Jun	1572	2933 2011
Jul	1020	1827 2023
Aug	676	1224 2011
Sep	317	571 2019
Oct	143	356 2014
Nov	43	96 2022
Dec	30	92 2021

Figure 4 presents a Hail Zone Map of the contiguous United States, based on the fifteen-year mean recurrence interval. The map categorizes regions by hailstone size, expressed in terms of diameter. The green-shaded areas represent moderate hail zones, where diameter of hailstones typically does not exceed 1.75 inches. In severe hail zones, hailstones can reach sizes of up to 2 inches. Additionally, parts of central America fall within very severe hail zones, where hailstones larger than 2 inches are expected [13].

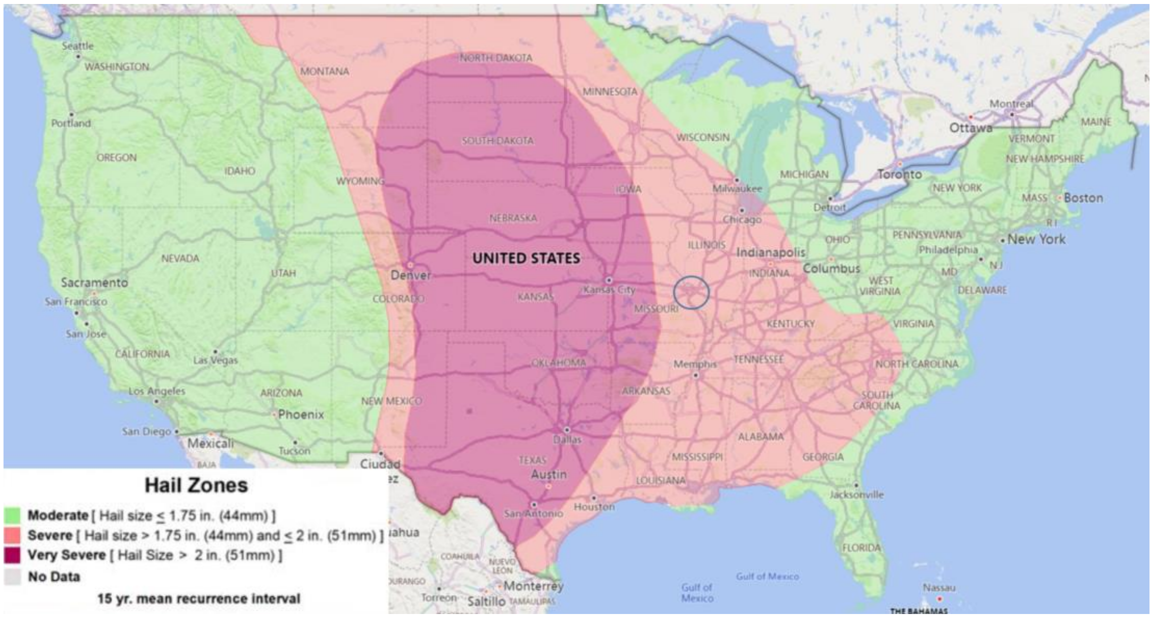

Figure 4 Hail Zones in the Contiguous United States [14]

Hail storms often carry hailstones of different sizes. For a hailstone with a diameter of 1.75in, the expected terminal velocity can be between 51 and 76mph. While determining the terminal velocity of a hailstone is very complicated, most empirical models predict that it will increases with size of the hailstone [15]. Figure 5shows a photo of the largest hailstone recovered in the United States. It has a diameter of about 8 inches, and the expected fall speed can be above 100mph [16]. In 2022 alone, 5879 severe hail events were reported in the United States [17]. Hail-related damages caused a $130 million annual client loss on average, according to FM Global [18].

Figure 5 Largest Hailstone Recovered in the U.S.

Chapter 2

Simulated Hail Impact Test Standards in the Roofing Industry

As was discussed in the previous chapter, hail events can cause significant damage to commercial roofing systems, leading to substantial financial losses. To mitigate these losses, property owners often rely on insurance coverage. When hail-related damage occurs, insurance providers are typically responsible for covering repair or replacement costs. As a result, insurers have a strong incentive to support and promote testing systems that help prevent or reduce such damage. This chapter discusses two of the most recognized impact resistance testing approaches in the roofing industry: the FM Global standard FM 4470 and the UL 2218A standard developed by UL Standards & Engagement, which were both developed by organizations sponsored by insurance companies (at the time).

2.1 FM 4470

The FM 4470 standard was first published in April 1986 [19] [20], under the title: "*Class 1 Roof Covers*", by the company then known as Factory Mutual Engineering and Research Corp. [21], to establish a series of roof cover testing standards. As part of the standard, a certification protocol for Moderate Hail (MH) was introduced to evaluate the hail impact resistance performance of roofing systems. In 1987, a Severe Hail (SH) rating was added through a supplement of FM 4470 [20], increasing the tested impact energy from 8 to 14 $ft \cdot lbf$. To address the growing threat of hailstorms producing hailstones exceeding 2 inches in diameter, FM Approvals further introduced the Very Severe Hail (VSH) rating in 2017 [22].

The current title of the standard is: "*Examination Standard for Single-Ply, Polymer-Modified Bitumen Sheet, Built-Up Roof (BUR) and Liquid Applied Roof Assemblies for Use in Class 1 and Noncombustible Roof Deck Construction*". The impact testing protocols are specified in Chapter 4.4 of FM 4470.

For MH certification, two identical samples must be prepared according to replicate the actual application scenario—one unconditioned and the other conditioned. Note that "conditioned" here actually refers to "weathered for 1000 hours in an Ultraviolet Weathering Cabinet" [23]. The two samples are then tested by subjecting them to a minimum of 10 impacts from a 2-in-diameter[1] steel ball dropped from a height of $81\ in.$ The resulted impact energy is $8\ ft \cdot lbf$. The procedure for SH certification is identical, except the drop height is increased to $141.5\ in.$, corresponding to an impact energy of $14\ ft \cdot lbf$. [23]

For VSH certification, lab-made ice balls are used as the impactor. The ice balls are produced using molds filled with distilled water. They are stored in a freezer for at least 48 hours at a temperature of $-7° \pm 7°$F. Each ice ball must have a mass between 0.1385 and $0.1524\ lbs$ and be free of cracks and air bubbles [24]. FM 4470 also requires the ice balls to have a $2 - in.$ diameter. Based on this dimension and weight, the density of ice was calculated to be $0.0331\ lb/in^3$.

In addition to the two types of samples required by the MH and SH certification, an additional sample is required for VSH testing. However, FM 4470 does not specify the

[1] The diameter of the steel ball was calculated based on the $1.19\ lb$ weight specified by FM 4470, using a steel density of $0.2841\ lb/in^3$, as the dimension was not provided.

conditioning requirement for this third sample[2]. The ice balls are propelled onto the samples with a launcher. The required number and location of impact are summarized in Table 2. An impact energy of greater than $53\ ft \cdot lbf$ is deemed acceptable, which is verified by measuring the velocity of the ice balls immediately before impact. [23]

Table 2 Impact Locations of Various Types of Roofing Assemblies [25]

Sample	**Impact Locations**
Fully adhered roof cover over mechanically fastened substrate	1 – field-fabricated seam 1 – field of roof cover 1 – fastener/stress plate
Fully adhered roof cover over fully adhered substrate	1 – field-fabricated seam 2 – field of roof cover
Fully adhered roof cover over partially adhered (ribbon applied) substrate	1 – field-fabricated seam 1 – field of roof cover directly over ribbon 1 – field of roof cover between ribbons
Partially adhered roof cover over fully adhered substrate	1 – field-fabricated seam 1 – field of roof cover directly over ribbon 1 – field of roof cover between ribbons
Partially adhered roof cover over partially adhered (ribbon applied) substrate	1 – field-fabricated seam 1 – field of roof cover directly over ribbon 1 – field of roof cover between ribbons
Mechanically fastened roof cover over loose laid substrate	1 – field-fabricated seam 1 – field of roof cover 1 – fastener/stress plate
All other assemblies	Minimum of three impacts at critical locations as determined by engineer.

[2] "For VSH three identical samples are prepared as above. Sample 1 is unconditioned. Sample 2 is either UV conditioned as above or heat aged."—FM 4470

The samples are then examined at the impact locations. Certification is granted if no tear in the field and no seam separation are observed under 10x magnification.

2.2 UL2218A

Another widely recognized impact test standard is the ANSI/UL 2218A. It was published by Underwriters' Laboratories on Aug 2, 2019 as a supplement to their UL 2218 standard, which focused on evaluating the impact resistance performance of steep slope roofing systems.

According to the standard, samples of representative roofing systems are assembled on a test deck, which is a $3\ ft \times 3\ ft$ square constructed from $15/32\ in.$ thick exterior-grade plywood fastened to a $2\ in. \times 4\ in.$ wood batten frame. An additional $2\ in. \times 4\ in.$ support runs across the midspan to increase rigidity. The samples have the same footprint as that of the test deck, and are conditioned according to the corresponding requirements. A device for releasing a steel ball of specified diameters (see Table 4) is outlined but not mandated, as long as consistency in impact locations and release heights is maintained. The impact locations vary depending on the configuration of the roofing system under test (Table 3). For each selected impact location, two instances of coincident impacts—measured to be within $0.5\ in.$ of each other—need to be performed [26].

After all impacts are completed, the top surface of the roofing system is visually checked for damage, aided by up to $5 \times$ magnification. If no signs of physical damage (tearing, cracking, rupture, etc.) are observed, the roofing system is rated according to the impactor used, ranging from Class 1 to Class 4 (Table 4).

2.3 Comparison and Discussion of Test Procedures

The key factors of the two test standards are summarized in Table 3 and Table 4. As shown, the industrial impact-resistance testing standards are essentially simulated hail impact tests. However, even the ice balls used in VSH tests do not perfectly represent natural hailstones. From an engineering standpoint, the use of steel impactors significantly reduces both the complexity and cost of testing. Also, for a given amount of impact energy, an ice ball may not inflict the same level of damage as a steel ball. Thus testing with steel impactors provides a conservative assessment of a roofing system's hail-resistance capability.

Another important consideration is the interpretation of test results. In mechanically fastened systems, it is relatively straightforward to examine potential damage across different layers. In contrast, for partially or fully adhered systems, such examination can be difficult or even impossible. This raises an important question: Do underlying components suffer structural damage even when the roof cover itself shows no visible failure? Addressing this issue requires further experimental investigation.

Table 3 Comparison of Impact Test Conditions in FM and UL Standards

	FM 4470		**UL 2218A**
Impact location	N/A	Table 2	Vulnerable such as edges, corners, unsupported sections and joints
Impactor	Steel ball	Ice ball	Steel ball
Aging considered	Yes	Yes	NO
Test deck size	—	—	$3ft \times 3ft$
Temperature	N/A	$40 - 45$°F	73.4 ∓ 7.3°F
Total points of impact	≥ 10	≥ 3	6
No. of impact per point	—	—	2

Table 4 Comparison of Impactor and Resulted Impact Energy in FM and UL Standards

	FM 4470				UL 2218A			
	Diameter ($in.$)	**Drop Height (ft)**	**Kinetic energy ($ft \cdot lbf$)**	**Rating**	**Diameter ($in.$)**	**Drop Height (ft)**	**Kinetic energy ($ft \cdot lbf$)**	**Rating**
Steel ball					1.25	12	3.53	Class 1
					1.5	15	7.35	Class 2
	2	6.5	8	MH				
					1.75	17	13.56	Class 3
	2	11.8	14	SH				
					2	20	23.71	Class 4
Ice ball	2		≥ 53	VSH				

Chapter 3

Impact Test of Fully Adhered and Non-adhered TPO Roofing Samples

This section describes the design philosophy of a customized drop tower developed to perform impact tests corresponding to FM 4470's Moderate Hail (MH) and Severe Hail (SH) certification procedures, as well as a simulated VSH test—in which the standard ice ball is replaced with a heavier metal impactor to maintain a practical drop height while achieving the desired impact energy.

The drop tower was used to perform impact tests on both fully adhered and non-adhered TPO roofing samples constructed in a benchmark configuration. The drop tower and components of this benchmark roofing system are described in this section, followed by a presentation of the observed test results from the impact experiments.

3.1 Drop Tower Design for MH, SH, and Simulated VSH Testing

The drop tower is a self-standing apparatus designed to release steel impactors from adjustable heights (Figure 6). It consists of a frame system constructed from anodized T-slotted aluminum rails (hereafter referred to as aluminum rails or simply rails, see Figure 7) built on top of a H-beam steel base. The base is a 77-inch-long segment of W12 × 190 capped at both ends with steel plates. On each flange of the H-beam, two rows of holes were drilled to mount short horizontal aluminum rails that serve as the base anchors for the frame structure. Three 10-foot-long aluminum rails (main columns) were mounted vertically onto the horizontal rails—two at the front side, one at the back. Their mounting positions were carefully selected to ensure that the required drop height for the SH test ($11.8\ ft$) could be achieved.

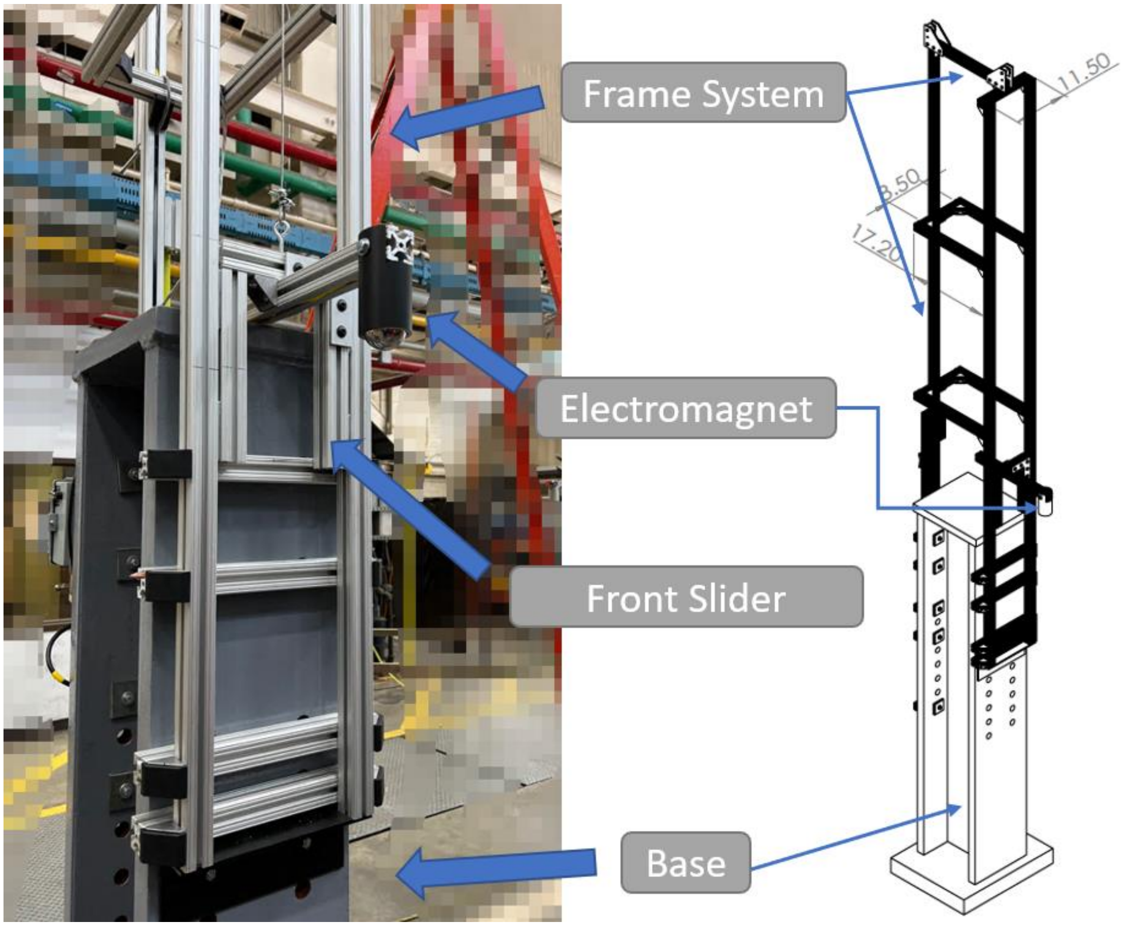

Figure 6 Overview of the drop tower assembly

Between the two front main columns, a sliding mechanism was assembled using aluminum rails arranged perpendicularly with each other to form a C-shaped frame (Figure 8). The open side of the "C" faces downward, allowing the two vertical members to be connected to the main columns through rail slides (Figure 9). Another piece of aluminum rail, vertically aligned on the back side of the drop tower, serves as the rear slider (Figure 10). This rear slider is also connected to the rear main column via three rail slides. These rail slides are equally spaced, with the one in the middle being a special rail slide with a cam handle (Figure 9). To facilitate manual repositioning, a bolt is installed horizontally near the bottom end of the rear slider. This bolt is oriented perpendicular to the rear slider and functions as a pull handle. A pull rope is tied to the bolt, allowing the operator to lower the rear slider by pulling on it when the rear slider is in its uppermost position and the pull handle is out of reach (Figure 10).

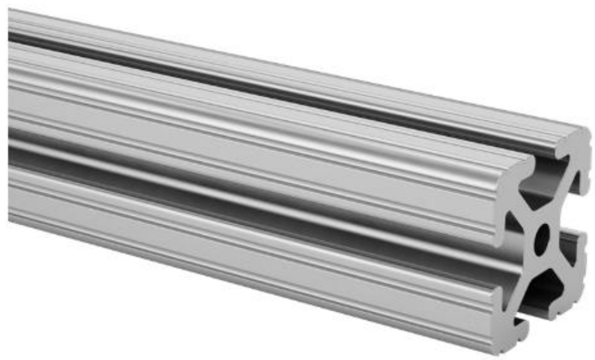

Figure 7 T-slotted Aluminum Rail [27]

To ensure structural stability, three sets of bracket beams were installed. The two lower sets are C-shaped, and the top set is T-shaped (Figure 6). The top bracket also supports two pulleys, over which a wire cable is routed to connect the front and rear sliders, enabling them to move synchronously.

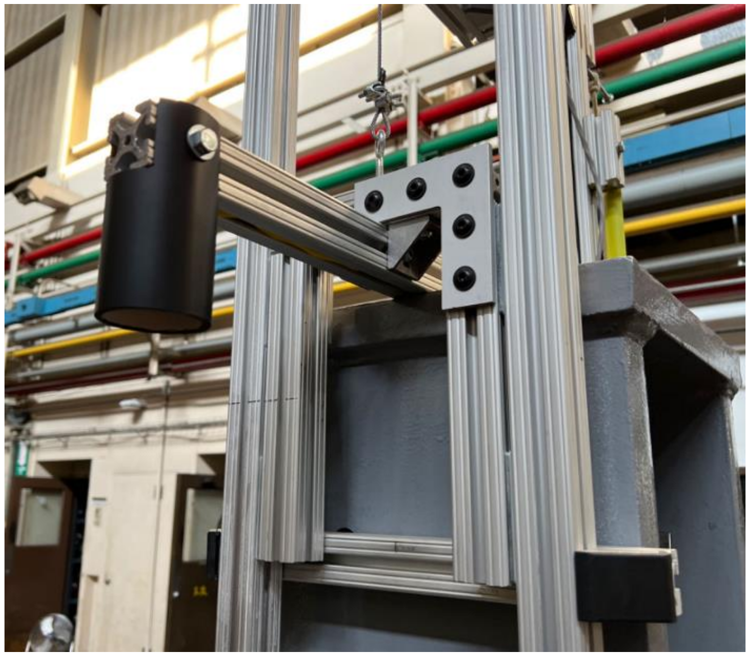

Figure 8 Front slider with impactor releasing mechanism

An electromagnet is mounted on the front slider to serve as the release mechanism for steel impactors. It is mounted on a horizontal rail with an adjustable extension, allowing control over the horizontal distance between the impact point and the base of the drop tower (Figure 8). The electromagnet is also covered with a short piece of PVC pipe cut into shape. This helps positioning the impactors so that they are aligned to ensure consistent impact. The electromagnet is wired to a control box that is mounted to the back side of the drop tower and can be switched on and off via a toggle switch (Figure 10).

Figure 9 Rail slide and slide with cam handle [28] [29]

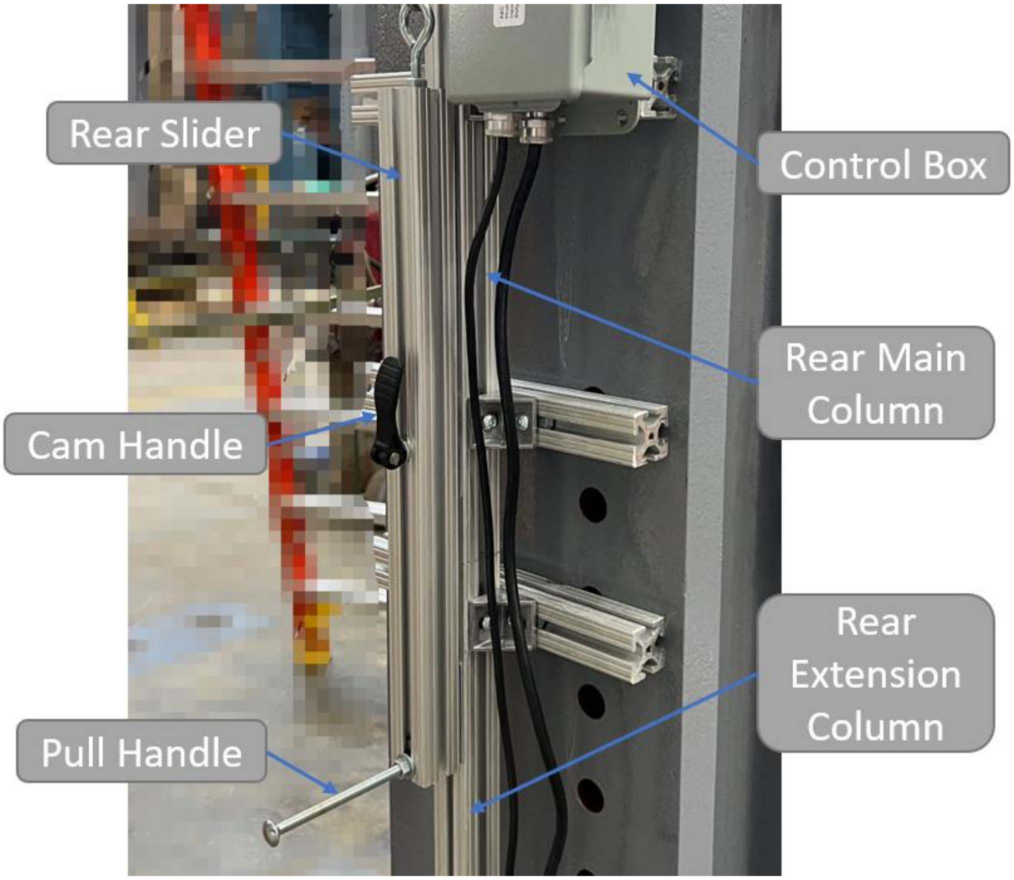

Figure 10 Rear slider

To assist with accurate drop height adjustment, a cut segment of tape measure was mounted vertically alongside the rear slider (Figure 11) as a height scale. This scale allows the operator to determine the current height of the impactor relative to the base of the tower, based on the vertical position of the rear slider. The position of height scale can be adjusted to accommodate the variation of the thickness of the sample to be tested. It provides a quick and reliable visual reference for setting specific drop heights required by different test standards.

The drop tower is capable of dropping a 2-in-diameter steel ball from 6.23 ft to 13.1 ft, covering the impact test height range of MH (6.5 ft) and SH (11.8) test specified by FM

4470. It can also handle impactors with smaller sizes with a change of the magnet cover to ensure alignment. The electromagnet is capable of holding the cylindrical impactor that weights 5.44 lbf.

Figure 11 Drop height scale

Most of the components used in constructing the drop tower were procured directly from commercial vendors such as McMaster-Carr. This helped simplify the construction process, reduce construction time, while also allowing it to be easily replicated. The dimensions of key components, particularly the lengths of the aluminum rails, were carefully selected to minimize material waste.

In accordance with the requirements of the research sponsor and collaborator, the drop tower was designed as a stand-alone structure, rather than an attachment to an existing wall or building. The tower was initially assembled and precisely adjusted in the Large Structures Laboratory of the ATLSS Engineering Research Center at Lehigh University's

Mountain Top Campus. Following the completion of impact testing at Lehigh, the drop tower was shipped to a testing facility of the sponsor, where it continues to serve as an efficient testing equipment.

Figure 12 The drop tower ready for its first test

3.2 Impact Testing of Roofing Assemblies: The Benchmark TPO Roofing System

The benchmark roofing system used as samples of impact testing is a fully adhered, single-ply roofing assembly with a thermoplastic polyolefin (TPO) membrane as the roof cover (Figure 13). The benchmark roofing system consists of three components: a TPO membrane, a cover board, and an Polyiso insulation board. The components are bonded together using a low-rise polyurethane (PU) foam adhesive, forming a laminated composite structure.

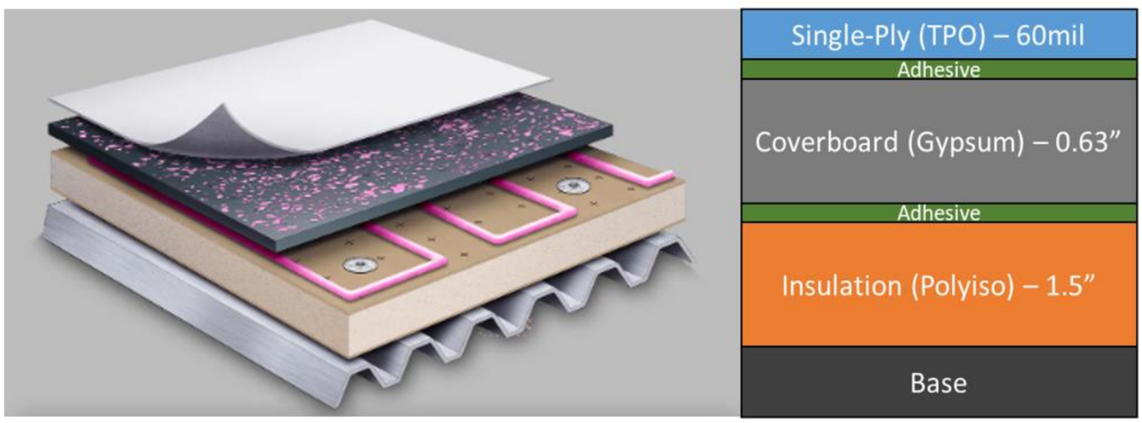

Figure 13 Schematic of the benchmark TPO roofing system [30]

The TPO membrane can be regarded as a three-layer component. The matrix material with the white color is referred to as the cap, for it’s the topmost layer of the roofing system to resist environmental elements such as sunlight and rain. The matrix material on the other side of the TPO membrane is referred to as the core. Between these two layers is a polyester scrim reinforcement, which provides dimensional stability and resistance to tearing [31]. Commercially available TPO membranes typically range from 45 mil to 80 mil in thickness. In this research, a 60 mil TPO membrane was used.

Figure 14 Samples of TPO membrane [32]

Directly beneath the TPO membrane is the cover board which is also a layered structure (Figure 15). The cover board consists of a gypsum core faced on both sides with glass mat facers. The upper surface with a dark-green color, is referred to as the top facer of the cover board (TFCB), while the opposite surface is the bottom facer (BFCB) (Figure 16). A knitted glass-fiber scrim is embedded between the gypsum core and the top facer, further enhancing the board's strength and dimensional stability. The cover board used in this study has a manufacturer-specified thickness of 5/8 in [33].

Beneath the cover board lies the polyisocyanurate (polyiso) foam insulation layer (Figure 7). This material is manufactured as foam blocks clad with identical glass fiber-reinforced cellulosic facers on both surfaces. Polyiso foam provides both thermal insulation and structural stiffness. The Polyiso insulation board used in this research has a thickness of 1.5in. The foam was reported to have a Young's modulus of approximately 772 psi (measured within ±4% strain) and an ultimate tensile strength of 22.63 psi [34].

Figure 15 Samples of cover board for bending test [32]

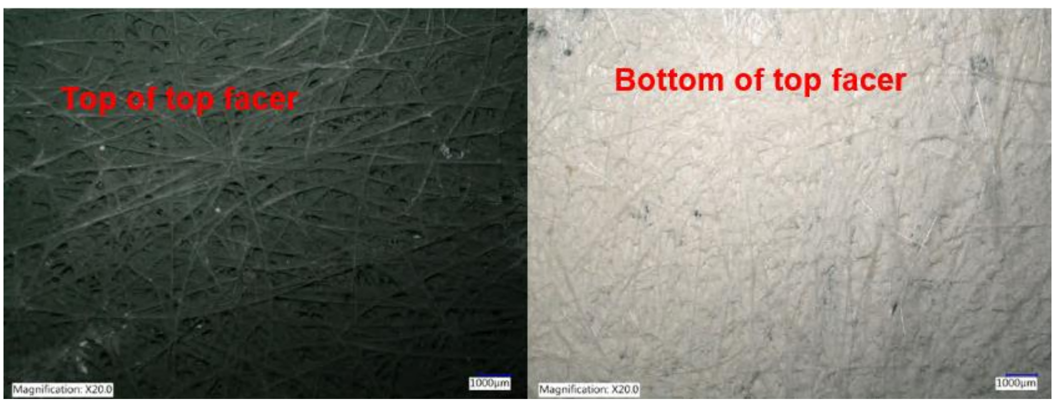

Figure 16 Top facer of coverboard

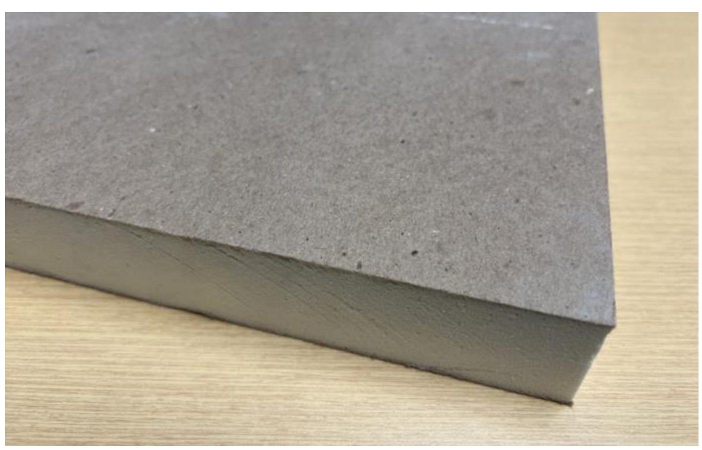

Figure 17 Polyiso insulation [32]

3.3 Impact Testing Setup

3.3.1 Roofing Samples

Roofing samples of two different configurations were utilized in the impact tests:

(1) fully-adhered with proper adhesives (assembled in a lab environment).

(2) non-adhered (layers stacked without applying adhesives) (Fig.2).

The non-adhered samples, in the absence of any interlaminar bonding, were included to enable direct assessment of isolated damage on surfaces of each component layer. All samples had a footprint of $10 \times 10\ in.$ Note that for the impact tests conducted, no structural roofing decks (like the corrugated steel deck shown in Figure 13) were included.

Figure 18 Fully-adhered (top) and non-adhered samples (bottom)

3.3.2 Impactors

In this study, impact tests were performed using two different spherical metal impactors. Their dimensions, weights, range of drop height and the associated impact energy is provided in Table 5. The testing conditions of FM 4470 regulated ratings are also included.

The steel ball utilized in the impact test has identical properties with the FM 4470 specified impactor. The steel dart is a 2-in-diameter cylinder with a 1-in-radius spherical head. It was used to achieve comparable impact energy that can be seen in the VSH test.

Table 5 Comparison of impactors

	MH	SH	VSH	Drop Tower	
Impactor	Steel Ball	Steel Ball	Ice Ball	Steel Ball	Steel Dart
Impactor Diameter $(in.)$	2	2	2	2	2
Impactor Weight (lbf)	1.19	1.19	0.14	1.19	5.44
Drop Height $(in.)$	81	141.5	Launcher	74.8~157.5	1.36~3.34
Impact Energy $(ft \cdot lbf)$	8	14	53-58	7.4~15.5	24.3~59.7

Figure 19 Steel dart and steel ball

3.3.3 Impact Testing Procedures

The impact test utilizing the drop tower described in Chapter 5.1. To begin each impact test, the prepared sample was placed on a concrete slab positioned directly in front of the drop tower. With the cam handle released, the front slider was lowered to its lowest position[3]. The steel impactor was then held against the electromagnet, while power was turned on so that the electromagnet holds the impactor in place. The front slider was then raised to the desired drop height, which was confirmed by reading the height scale mounted on the rear column. Once the correct height was reached, the cam handle was re-engaged to lock the sliders in position. The electromagnet was then powered off, causing the impactor to drop freely onto the sample below.

Impact tests conducted using the steel ball were relatively safe. However, tests involving the steel dart posed a significantly higher safety concern. Upon impact, the dart was occasionally reflected upward to heights approaching $5\ ft$. A protective enclosure was constructed and positioned around the sample area. The enclosure was assembled from several thick plywood panels, each lined on the inner surface with foam sheets to protect the operator.

Each sample, due to their relatively small size, were only subjected to impact for once. After the tests were completed, the samples were first examined for damages on the TPO membrane surface. The operator would identify the impacted area and use a marker to circle out the dented area. For non-adhered samples, this procedure were repeated for every other surface: top and bottom surface of the cover board, top and bottom surface of the polyiso insulation board. The samples were then cut open along a straight line passing

[3] The front slider was deliberately constructed to be heavier than the rear slider.

the identified center of the impact to expose the damage inside the components. Damage conditions were then photographed and recorded.

3.4 Impact Test Results

All impact tests conditions of the tests performed using the steel ball are summarized in Table 6. Those using the steel cylinder are summarized in Table 7. They contain the drop height $h\ (in.)$, theoretical impact speed $v\ (ft/s)$ and the impact energy $E_i(ft \cdot lbf)$.

Table 6 Test conditions with 2-in-diameter steel ball

No.	$h\ (in.)$	$v\ (ft/s)$	$E_i(ft \cdot lbf)$.
B1	78.81	20.55	7.80
B2	88.81	21.82	8.79
B3	98.81	23.01	9.78
B4	108.81	24.15	10.77
B5	118.81	25.23	11.76
B6	128.81	26.27	12.75
B7	138.81	27.27	13.74
B8	148.81	28.40	14.72
B9	158.81	29.17	15.72

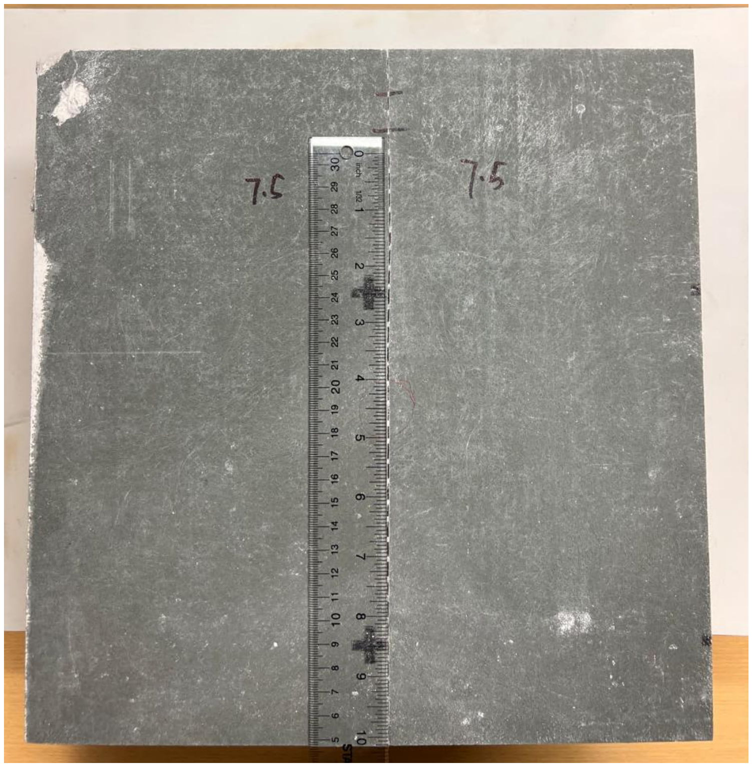

Figure 20 Non-adhered cover board was cut open along the center of the impact

Table 7 Test conditions with 2-in-diameter rounded cylinder

No.	$h\ (in.)$	$v\ (ft/s)$	$E_i(ft \cdot lbf).$
C1	49.7	16.32	22.50
C2	53.7	16.96	24.31
C3	57.7	17.58	26.12
C4	65.7	18.76	29.75
C5	73.7	19.87	33.37
C6	89.7	21.92	40.61
C7	133.4	26.74	60.40

3.4.1 Damage to the TPO Membrane

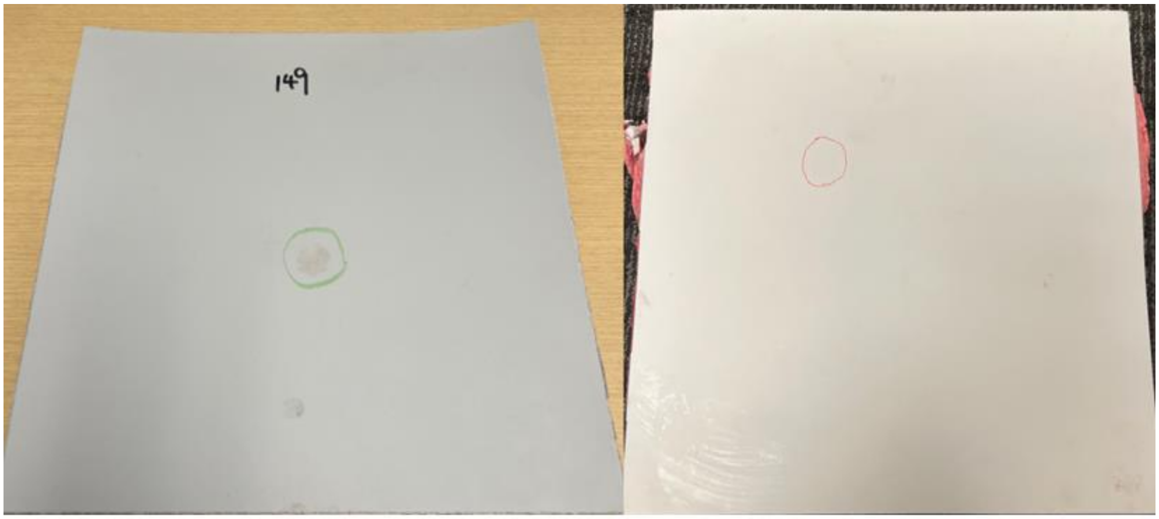

(a) (b)

Figure 21 Surface conditions of TPO membranes after impact

(a) B8, non-adhered sample (at E_i of SH test)
(b) C7, fully adhered sample (at maximum E_i tested)

Figure 21 shows the conditions of the top surface of the TPO membrane after the B8 and C7 tests. As illustrated in Table 6, the B8 test used the steel ball impactor on a non-adhered sample, resulting in an impact energy of $14.72\ ft \cdot lbf$, which is very comparable to that of the FM SH test. No visible damage was observed[4] on the TPO. Figure 21(b) shows the TPO membrane of a fully adhered sample after the C7 test, which used the steel cylinder. The C7 test had the highest impact energy among all the tests that were performed. Even at $E_i = 60.40\ ft \cdot lbf$, the TPO membrane remained intact. This impact energy is slightly greater than that specified by the FM VSH test.

The TPO membrane consistently withstood impact without fracturing across all tests. This result is consistent with the observations of Boardman and Brown [35], who reported that tearing does not typically occur in TPO membranes during field impacts[5]

[4] The "mark" inside the green circle was stains left by the impactor.

[5] A field impact denotes an impact landing on the unobstructed membrane surface, rather than on seams or washer plates.

when a cover board is present in the roofing system. In another research involved FM 4473 impact tests using ice balls, TPO membranes of various thickness fully adhered to gypsum cover boards also demonstrated strong performance and were highly evaluated [36].

3.4.2 Damage to the Facers

The bottom facer of the cover board (CBBF) did not exhibit visible cracking until the impact energy E_i was increased to $26.12\ ft \cdot lbf$ (test C3). In Figure 22 (C3), two small cracks, each approximately $0.5 in.$ in length, can be observed. These cracks extended in the radial direction. When the drop height was increased to $65.7 in$, (Figure 23, C4), a single crack measuring approximately $1.5 in.$ appeared. It was also aligned in the radial direction. Upon further increasing the drop height to $73.7\ in$, the cracks notably longer, while still following the radial direction. In test C7 (Figure 24), the BFCB exhibited severe damage with even longer cracks.

These observations suggest that the cracks in the CBBF were likely initiated at the center, directly beneath the impact region, and propagated outward in the radial direction. On the left of Figure 24, the top facer of the Polyiso insulation (PTF) is also shown. Cracking in the TFP was only observed during test C7, and the pattern of the cracks was very similar to those in the BFCB. The cracks appear symmetric in in Figure 24, as the BFCB and TFP were positioned opposite to each other during the impact test.

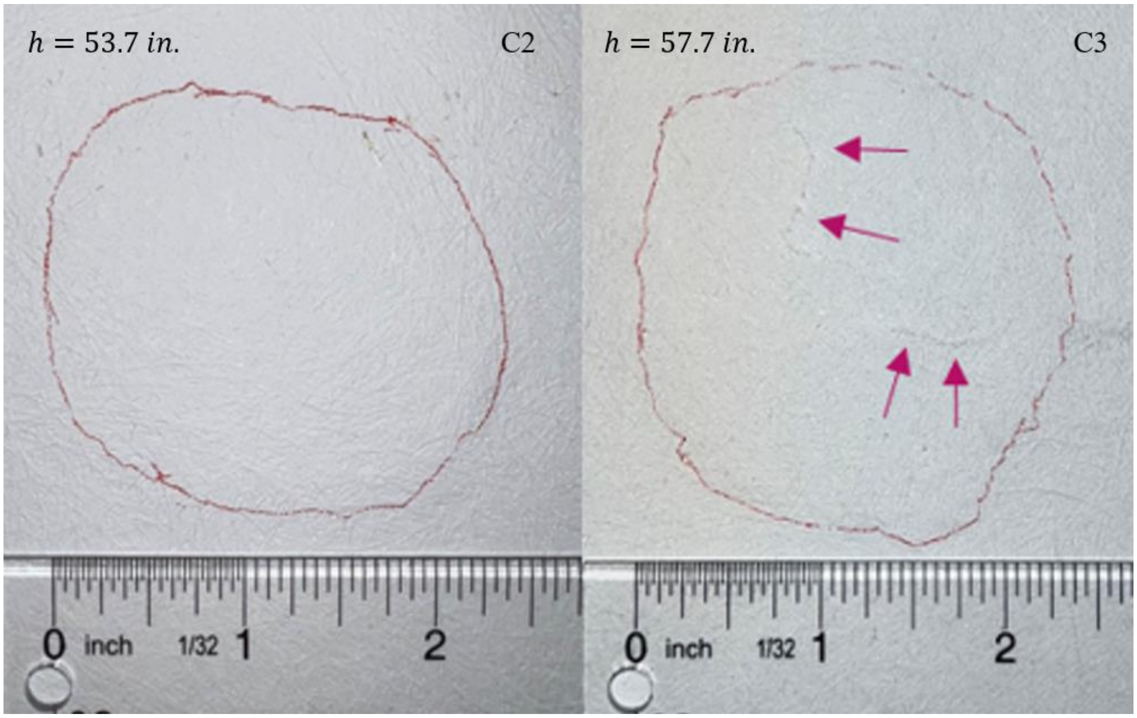

Figure 22 Cracks on BFCB, $h = 53.7in.$ & $h = 57.7in.$

As for the top facer of the cover board (CBTF), cracks were observed only in test C7. For those B-series tests, indentations were barely noticeable. From test C1 to C6, a circular indentation could be observed on the CBTF surface. As the drop height increased, the size and depth of the indentation also increased. In Figure 25, the indentation regions are highlighted with markers. The cracks pattern observed on the CBTF appears circular in shape.

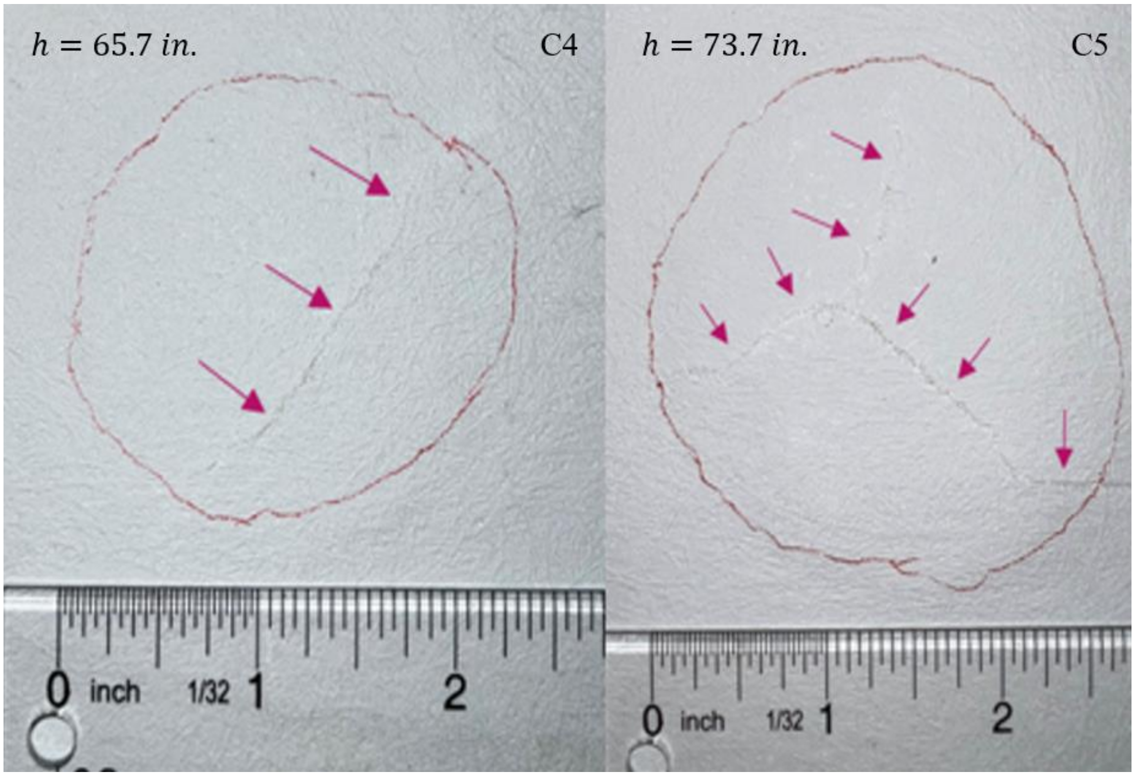

Figure 23 Cracks on BFCB, $h = 65.7in.$ & $h = 73.7in.$

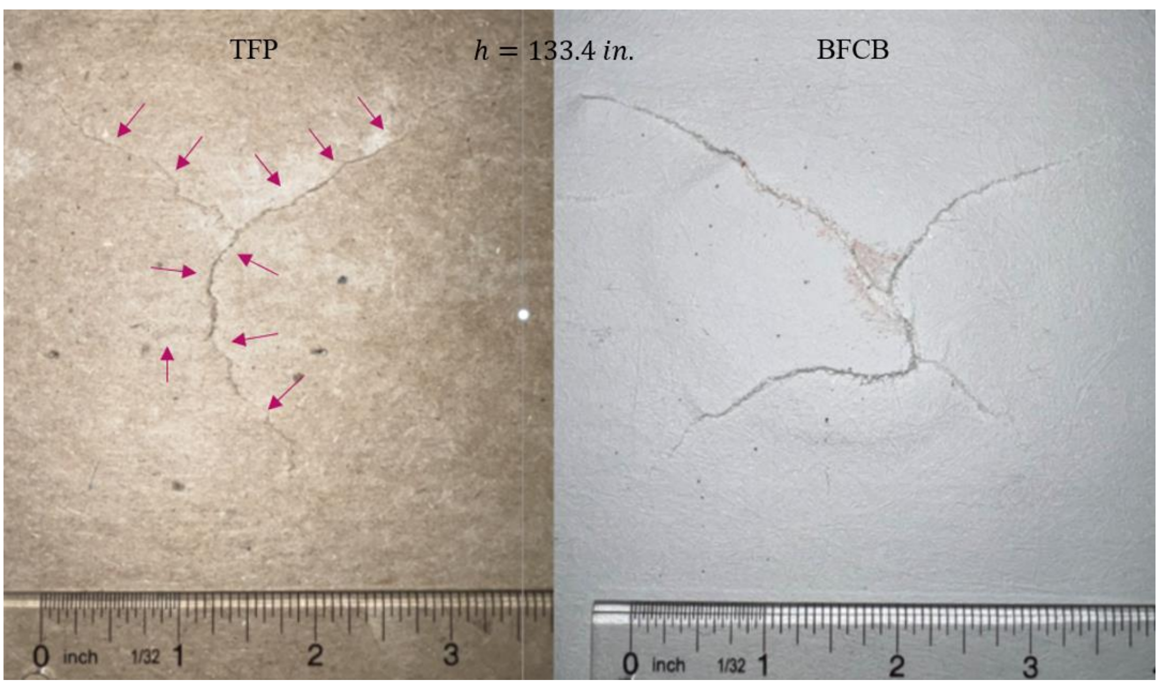

Figure 24 Cracks on BFCB and TFP, $h = 133.4in.$

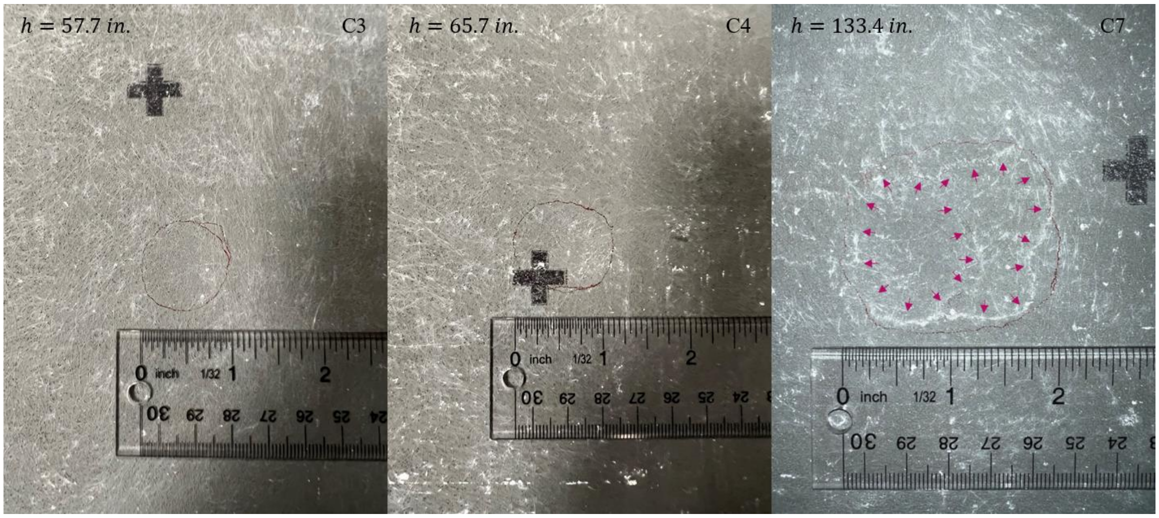

Figure 25 Indentation and cracks observed on TFCB

3.4.3 Cracks in the Gypsum Core

The cover-boards of non-adhered samples were also sectioned through the thickness direction to examine internal damage to the gypsum core at the impact location. At $h = 53.7\ in$ (C2, $E_i = 24.31 ft \cdot lbf$), no surface cracks were visible on either facer of the cover board. However, cone-shaped cracks, which are axisymmetric, were observed within the gypsum core, as highlighted in Figure 28 (C2) and (C3). These cone cracks exhibit characteristics of the *Hertzian cone cracks*, first described by Heinrich Hertz in 1881 during his research on the indentation of a hard spherical indenter on a flat glass specimen [37].

Subsequent drop tests revealed that such cone cracks could form within the gypsum core even at the lowest tested impact energy, $E_i = 7.80 ft \cdot lbf$ (Figure 26). As the impact energy increased, both the severity and number of cracks also increased. Across all the tested impact energy levels, the cone cracks extended from the top surface to the bottom surface of the gypsum layer, and caused delamination between the gypsum core and the bottom facer of the cover-board.

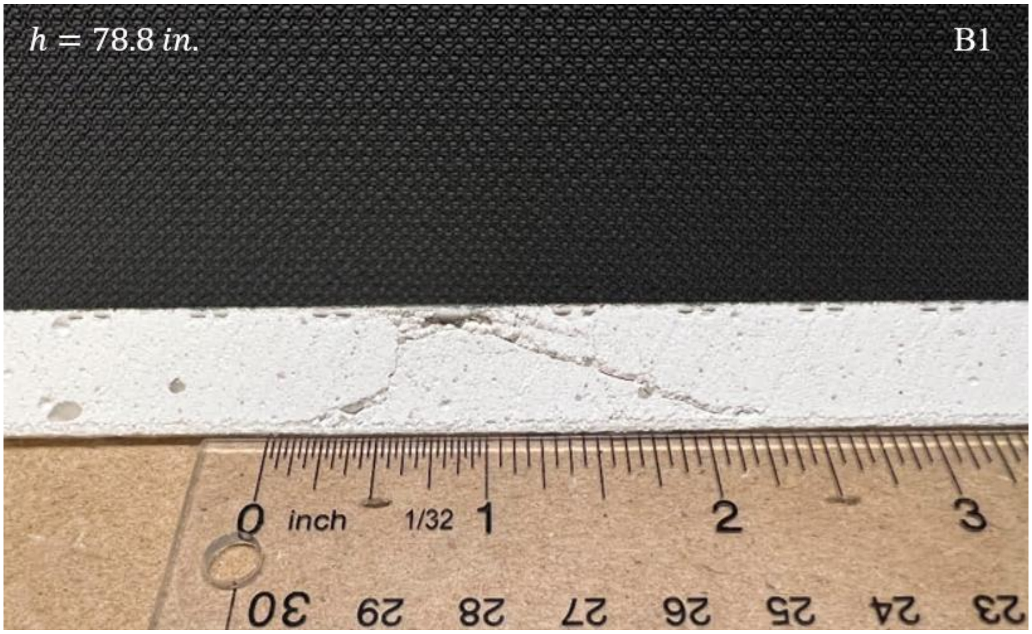

Figure 26 Cone cracks in the gypsum core, test B1

"Minor" cracks were also observed inside the cone-shaped cracks, such as the ones that are circled in Figure 28 (C4). Cracks like the ones shown in this figure corresponded more closely to the cracks observed on the exterior surface of the bottom facer of the cover-board, as seen in Figure 27, where the two internal cracks pointed out inside the gypsum layer were exactly aligned with the surface cracking on the bottom facer. This suggests that the cone cracks and the minor internal cracks likely originate independently. This will be further discussed in the finite element simulation section.

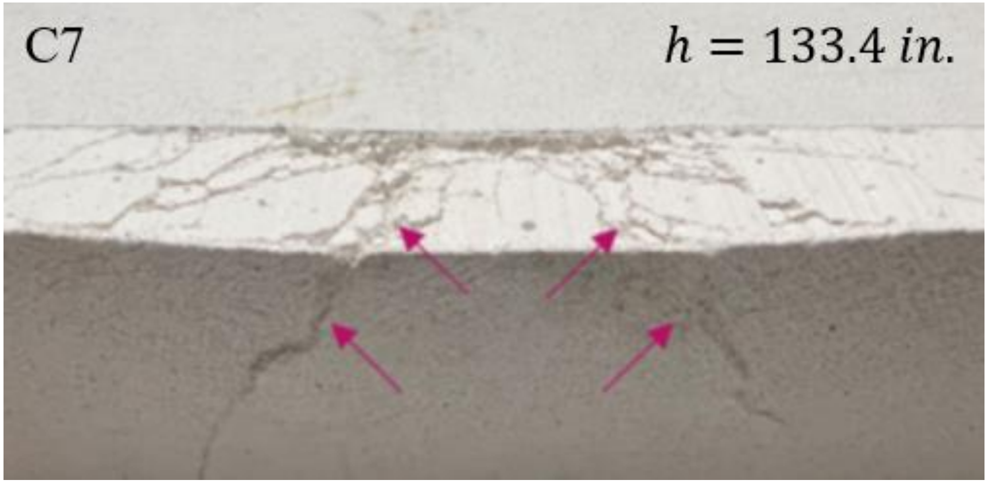

Figure 27 Cracks initiated on BFCM eventually extended into the gypsum core

The observed damage within each component of the non-adhered samples is listed in Table 8.

Table 8. Critical drop heights for observable damage in non-adhered samples

h (in)	CBTF	GC	CBBF	TPO	PTF
49.7		C			
53.7		C	C		
57.7		C	C		
65.7		C	C		
73.7		C	C		
89.7		C	C		
133.4	C	C	C		C

C: Visible cracks observed

CBTF: Cover-board top facer

GC: Gypsum core of cover-board

CBBF: Cover-board bottom facer

TPO: TPO membrane

PTF: Polyiso insulation top facer.

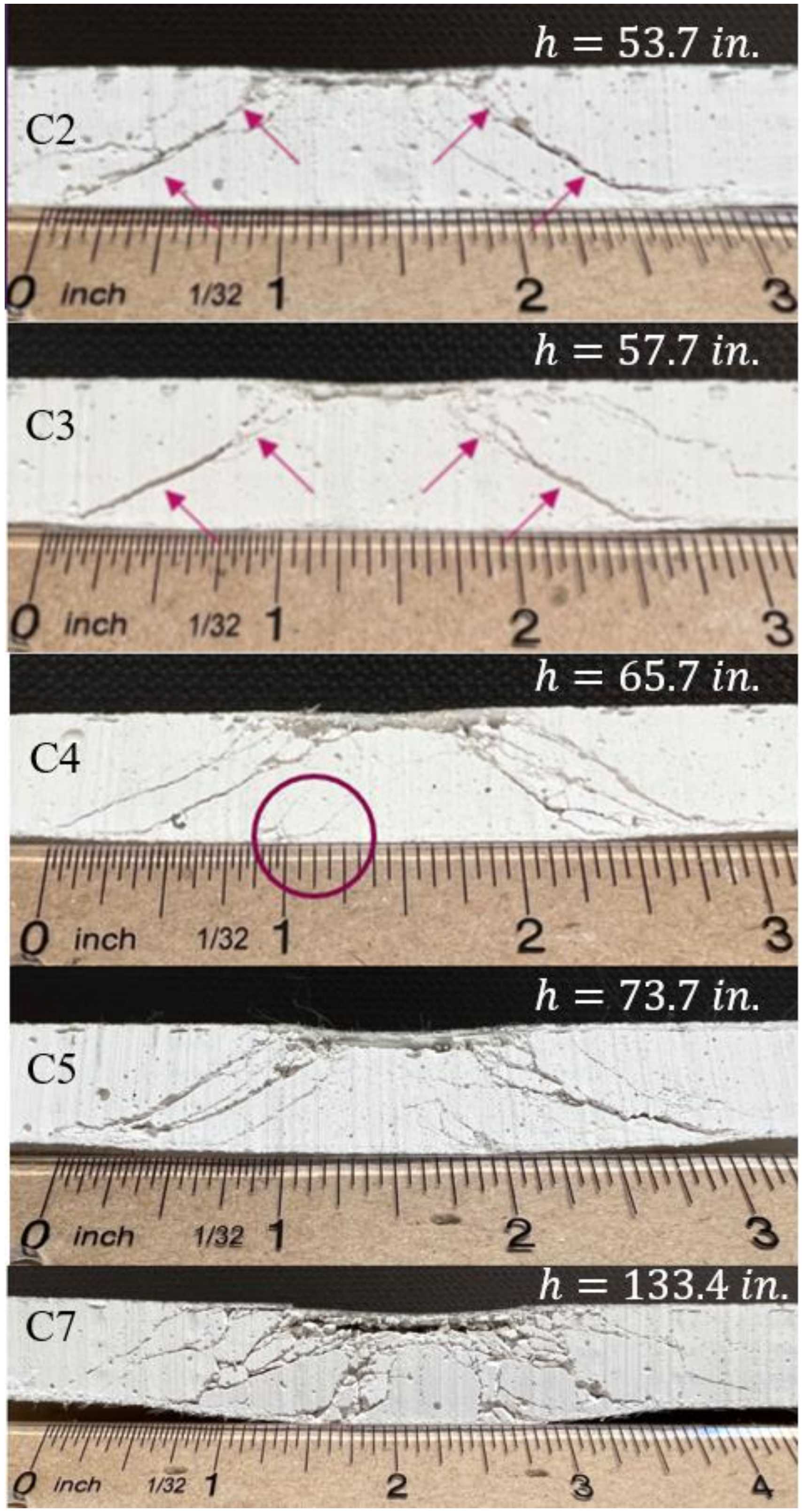

Figure 28 Cracks inside the gypsum core of cover board

3.4.4 Angle of Hertzian Cone Crack

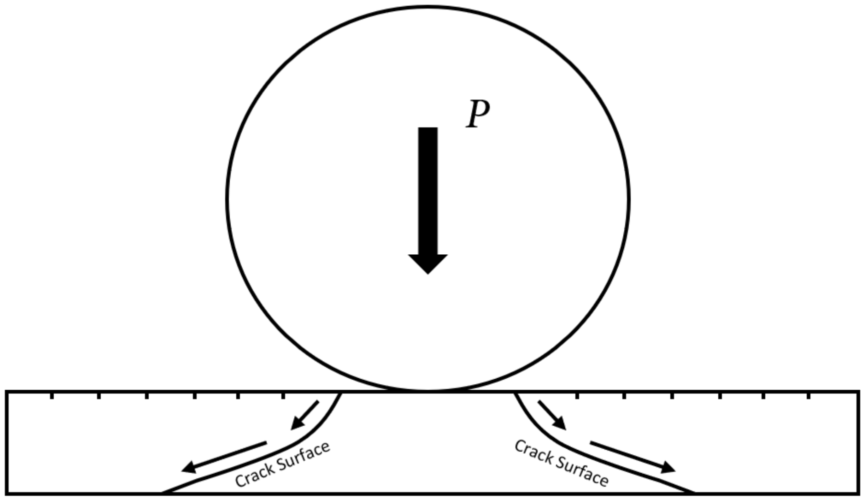

Figure 29 Schematic of Hertzian cone crack

Figure 29 presents a schematic drawing of a *Hertzian cone crack*. This type of crack typically forms within brittle materials during the indentation process by a hard spherical indenter, or under impact events. It is now widely accepted that the cone crack initiation is triggered by pre-existing surface flaws near the contact region. Based on this mechanism, Kocer and Collins [38] used finite element simulations to get a cone crack angle[6] of approximately 22° for soda-lime glass, which was in good agreement with experimental results. Their research suggested that the direction of the cone crack propagates in the direction of maximum strain energy release, rather than along the direction of the minimum principal stress [39].

The cone crack angles observed in this study are summarized in Table 9. As on the sectioned plane, the cracks were not perfectly symmetric, the cone crack angle was measured and reported on both sides.

[6] Defined by the acute angle between the crack surface and the top surface of the specimen.

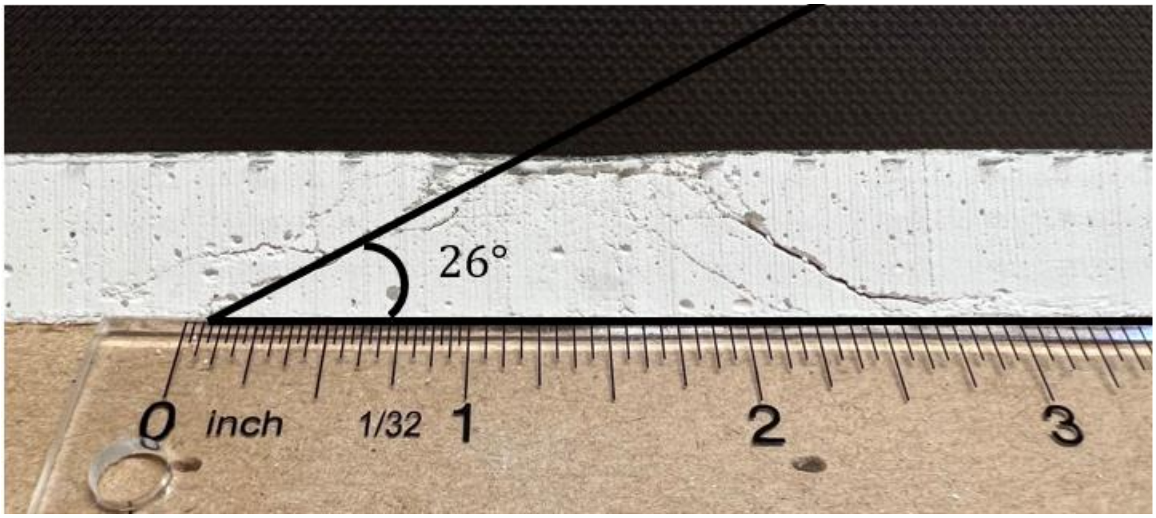

Figure 30 Cone crack angle

Table 9 Cone Crack Angle of the Cover Board Gypsum Core

	Left (°)	Right (°)
B1	29.4	21.2
B4	11.2	29.5
B8	26.0	29.1
C2	26.1	29.1
C3	26.9	30.0
C4	28.0	32.3
C5	22.8	16.9
C7	41.2	34.1

Chapter 4

Finite Element Simulation of the Impact Test

Observations from the impact tests suggested that the gypsum cover-board in the roofing system was the component most susceptible to facer and core material damage when subjected to impact from the spherical indenter. In order to better understand the cause of the damage, a series of finite element simulations were carried out using the ANSYS Mechanical modeling suite [40]. In this study, simulation of the drop test utilized quasi-static simulations, where the indenter displacement was specified through a sequence of time steps. The key assumptions in the quasi-static model are that the kinetic energy from the spherical indenter is completely converted to elastic strain energy in the layered roofing structure and the time of contact between the indenter and the structure is greater than the 1st natural period of the structure. Inertia effects can be considered to be negligible if the mass of the layered system is relatively low and wave propagation effects do not significantly alter the local stress state underneath the indenter. In addition, it was assumed that the material properties did not depend strongly on the loading rate.

4.1 Material properties

The TPO membrane used in the benchmark roofing system is a composite material consists of three layers: the cap layer (white), the scrim layer, and the core layer, with a total thickness of 60mil. Tensile tests of samples of the TPO membrane, as well as samples of the cap and the core alone were performed. Since the performance of the TPO membranes was not the concern, the stress-strain behavior of the TPO was documented, but was simulated as an isotropic elastic material base on the curve fitting results in the relatively low strain range (≤ 10%) to simplify the simulation.

Table 10 Typs of TPO samples tested

LNS	Lab made TPO, cap+core, no scrim
LM	Lab made TPO, cap+core+scrim, machine direction
LT	Lab made TPO, cap+core+scrim, Transverse machine direction
LW	Lab made TPO core
LB	Lab made TPO white
PM	Plant extruded TPO, cap+core+scrim, machine direction
PT	Plant extruded TPO, cap+core+scrim, transverse machine direction

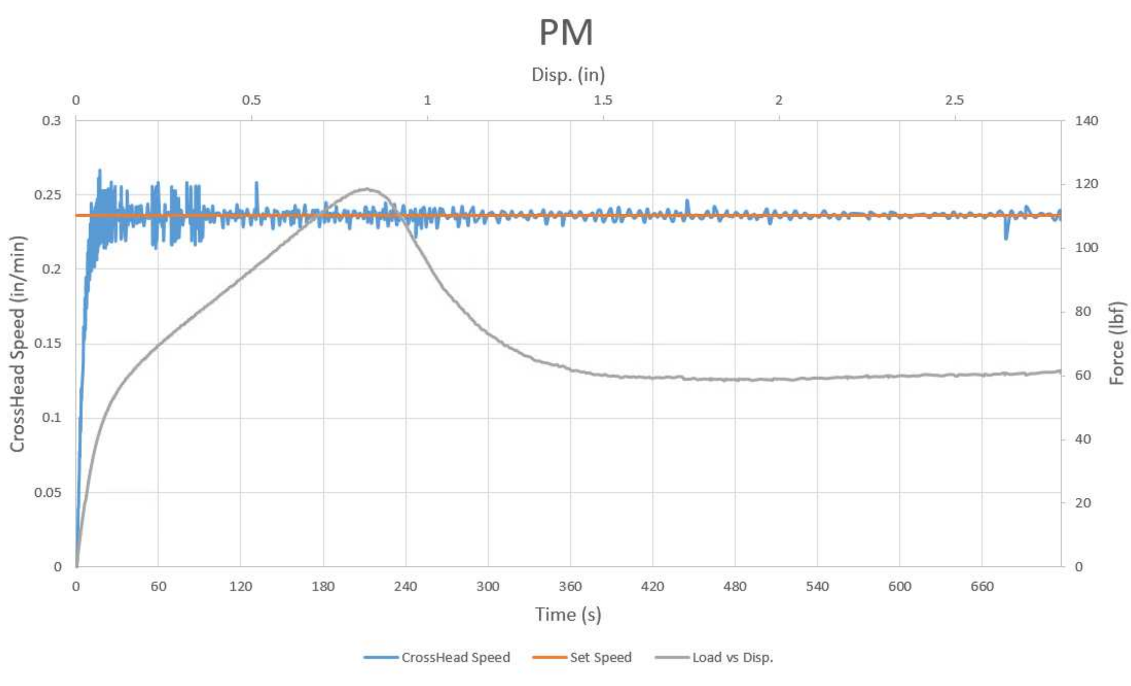

Figure 31 PM tensile test force-displacement curve vs crosshead speed and experiment time

Sample	Failure Disp.	Failure Load
1	-0.40678	-103.16247
2	-0.34799	-93.53194
3	-0.34060	-98.02888
4	-0.30524	-90.49111
5	-0.30006	-92.40416
6	-0.33881	-101.58628
7	-0.31467	-97.27177
8	-0.31072	-102.90583
9	-0.37189	-78.53327
10	-0.29540	-68.35808
11	-0.29835	-69.26129
12	-0.31072	-67.93731
13	-0.28660	-65.27052
14	-0.28233	-64.64469

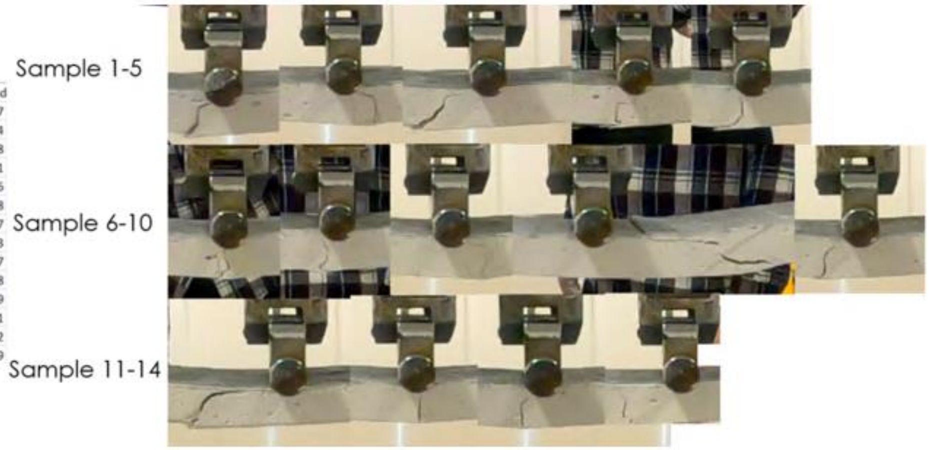

Figure 32 Cover board cracks during 3-point-bending tests

The cover board is also a layered structure. As direct access to the gypsum was not possible, 3-point-bending (3PB) test results was used to calibrate an FEA simulation of such a test, with measured tensile properties of the facers. Since the behavior of the cover board in a 3PB test is very sensitive to the thickness of the cover board, measurements were performed to validate the manufacturer claimed thickness. It turned out that, for the samples that were available, the average thickness of the coverboard was 602.49mil, approximately 3.6% thinner than that was claimed (625mil, $5/8\, in$). The samples of top and bottom facer were acquired by using a bend saw to cut a thin layer of gypsum together with the undamaged facer from the cover board. Since gypsum is a brittle material that cracks at a very low strain. When the gypsum layer left on the facer samples was thin enough, the effect to the tensile behavior to the facers are negligible. Both facers were measured to have a thickness of 6mil.

Figure 33 Lab-made CBBF sample tested

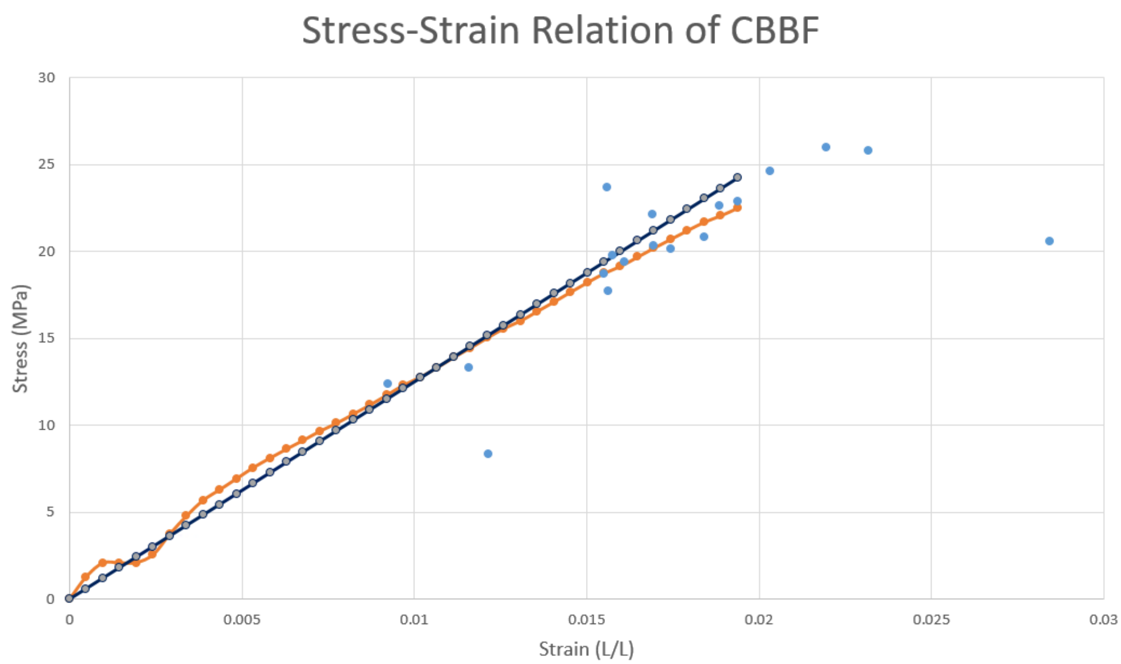

Figure 34 Stress-strain curve of the bottom facer of cover board

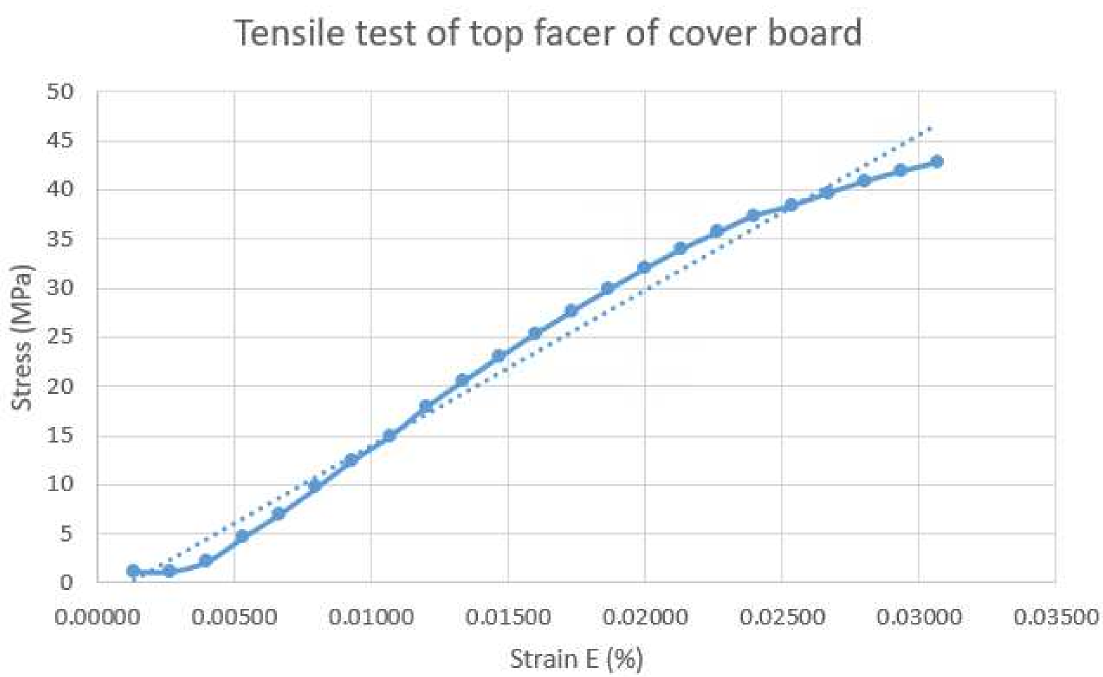

Figure 35 Curve fitting of the top facer of the cover board with scrims before break

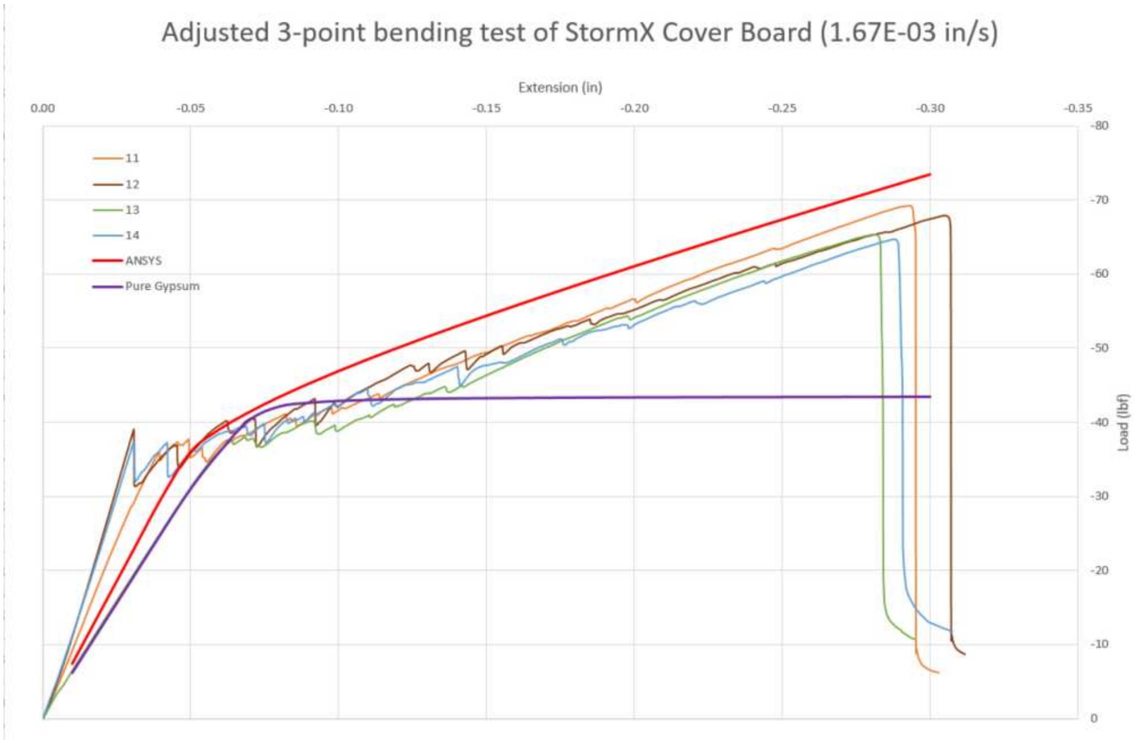

Figure 36 Force-disp. curve comparison between simulated and real 3PB test

Table 11 Material properties for FEA

Material	Young's Modulus (GPa)	Poisson's Ratio	Thicknes (mm)
TPO	0.299	0.3	1.524
CBTF	2.534	0.2	0.6
Gypsum	2.5	0.3	15.303
CBBF	1.25	0.2	0.6
Polyiso Foam	5.328e-3	0.25	38.1
PTF & PBF	14.619	0.3	0.0472
Indenter	200	0.3	

The Polyiso insulation board was also modeled as a layered composite material. The facer of the insulation board was provided, so its elastic modulus was acquired through tensile tests. Elastic modulus of the Polyiso foam was adopted from a previous research on the impact behavior of another TPO roofing system, by Tianyi Luo and Herman Nied [34].

Material properties adopted in the simulate are summarized in Table 11. All the materials were modeled as linear, isotropic materials.

4.2 Model Size and Boundary Conditions

The modeling of the simulation started with the scope of simulating the static indentation process with a spherical indenter of the benchmark TPO roofing system that characteristic the size of the samples utilized in the impact test. The model made use of the symmetry conditions of the impact test samples and the impactor, to first reduce the full-size model into a quarter model. It possesses one fourth of the volume of the roofing samples. The indenter was a half model of a quarter sphere to enable indentation control. But it was soon realized that the balance between mesh refinement and model performance need to be concerned. Since in controlling the indentation process, the strain energy is the factor selected to be the main consideration, a simulation with a focus on the strain energy distribution among different components and different regions of a single component was carried out. It was shown that the region within a radius of 3 inches of the indentation center (referred to as the inner region in Figure 37) bears over 96.15% of the total strain energy in the system. Thus, it was then decided to reduce the dimension of the roofing system from a 10-inch square shape to 3-inch disk. The adopted dimension of the model is shown in Figure 38. Table 11 shows the detailed arrangement of all the layers underneath the indenter: that are, from top to bottom, TPO membrane (TPO), cover-board top facer (CBTF), cover-board gypsum layer (GYP), cover-board bottom facer (CBBF), polyiso insulation top facer (PTF), polyiso foam layer (Foam) and polyiso insulation bottom facer (PBF).

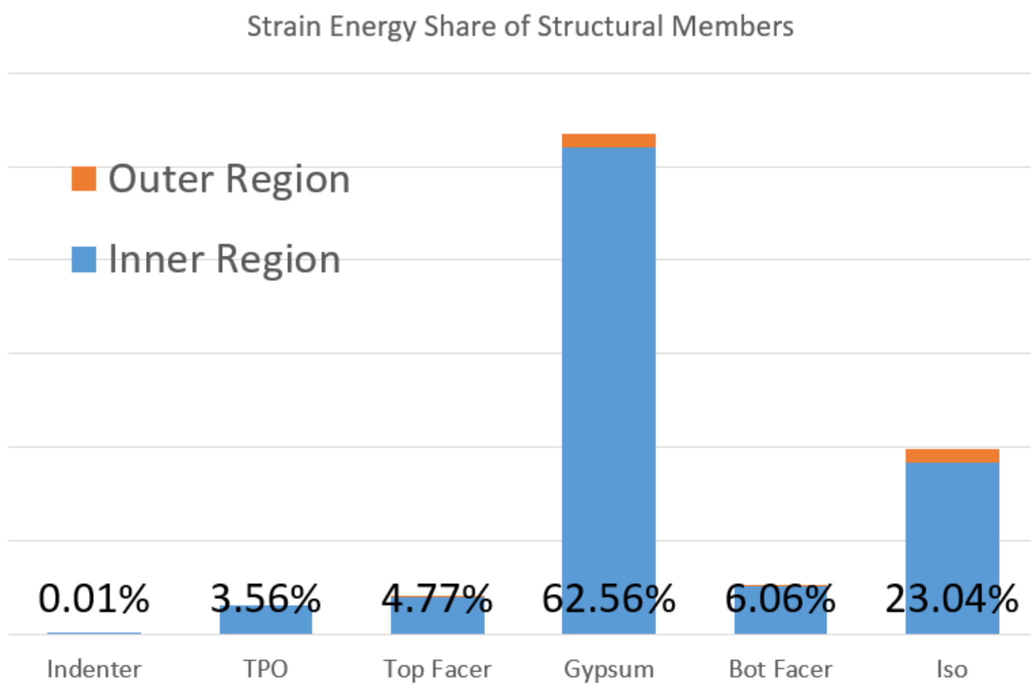

Figure 37 Strain energy of the inner and outer region of the full-size quarter model

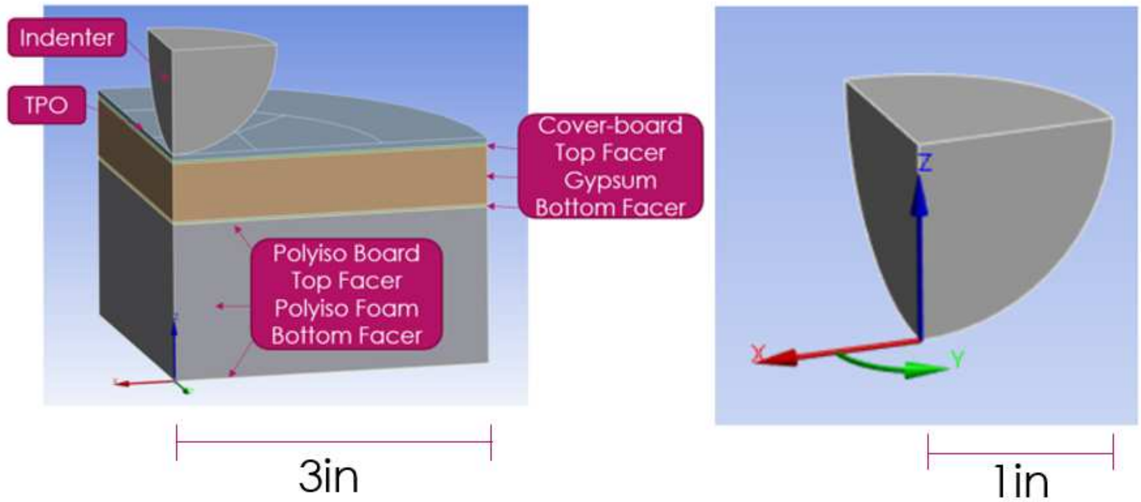

Figure 38 Dimensions of simulated roofing system and the indenter

Boundary conditions preventing translational deformation about the symmetry planes were applied on corresponding boundaries with the model fully supported in the z-direction. All surfaces between substrate layers are modeled as perfectly bonded, i.e., a fully adhered system. Both a fixed or a free circumferential boundary condition and the rough and frictionless contact between the indenter and the TPO membrane were tested. Any combination between the two group showed little effect on the strain energy distribution of the model.

The indentation process was controlled, as mentioned, by applying a vertical displacement along the negative z-axis at the top surface of the modeled indenter. Since the steel indenter carried a strain energy less than 0.01% of the system total strain energy, the actual size or the deformation far from the contact region should not affect the deformation and the stress distribution of the roofing components.

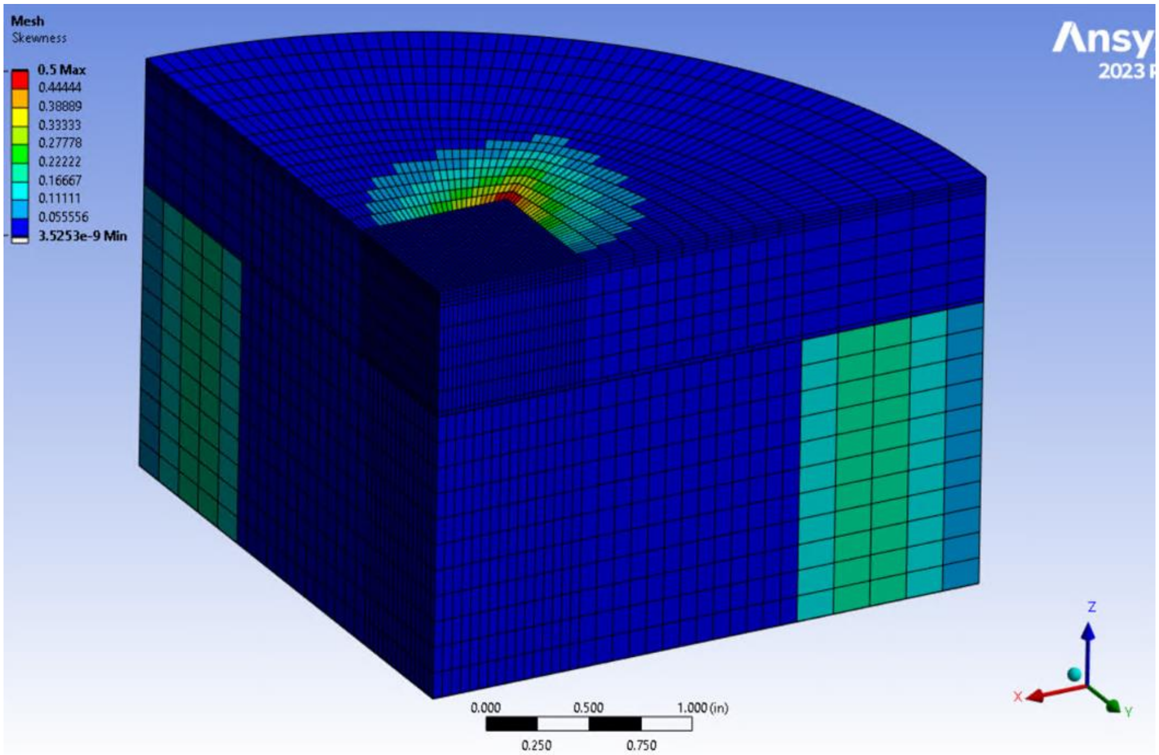

Figure 39 Mesh of the roofing system

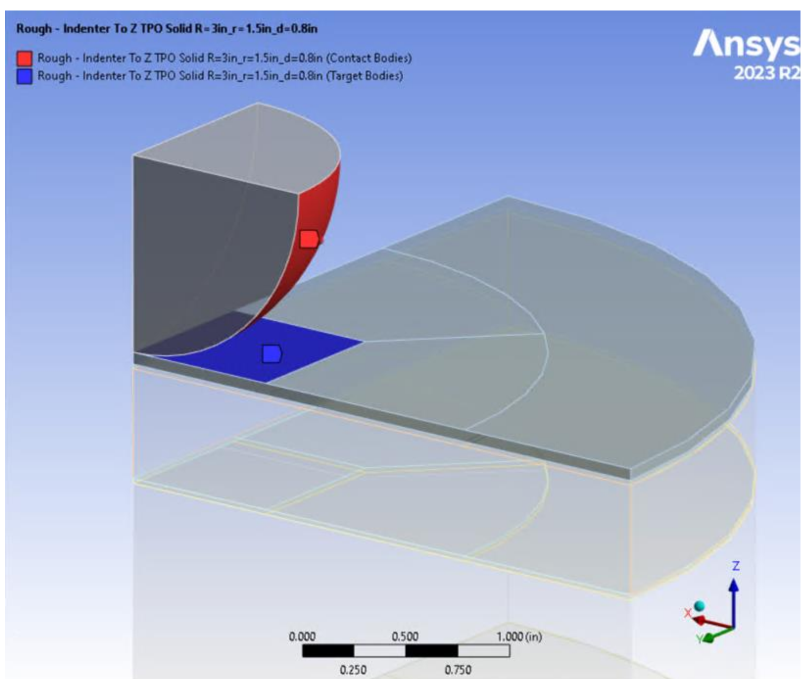

Figure 40 Rough contact between the indenter and the TPO membrane

4.3 Comparison of Simulation and Test Results

With the FEA simulations established, the computed elastic strain energy corresponding to different indentation depths, was compared with the measured kinetic energy of the impactor. A portion of this energy is lost due to irreversible processes associated with plastic deformation, creation of new crack surfaces, and frictional damping during the impact test. However, much of the elastic strain energy is recovered as the impactor velocity is reversed and the impactor rebounds from the test specimen. At the impactor's deepest point of penetration, i.e., when the vertical speed of the impactor is zero, the strain energy of the impactor-roof system is at its maximum. Figure 41 shows the relation between the indenter displacement Δz and the elastic strain energy obtained from the FE simulation. The strain energy can then be used to find the corresponding drop height that corresponds to the indentation depth.

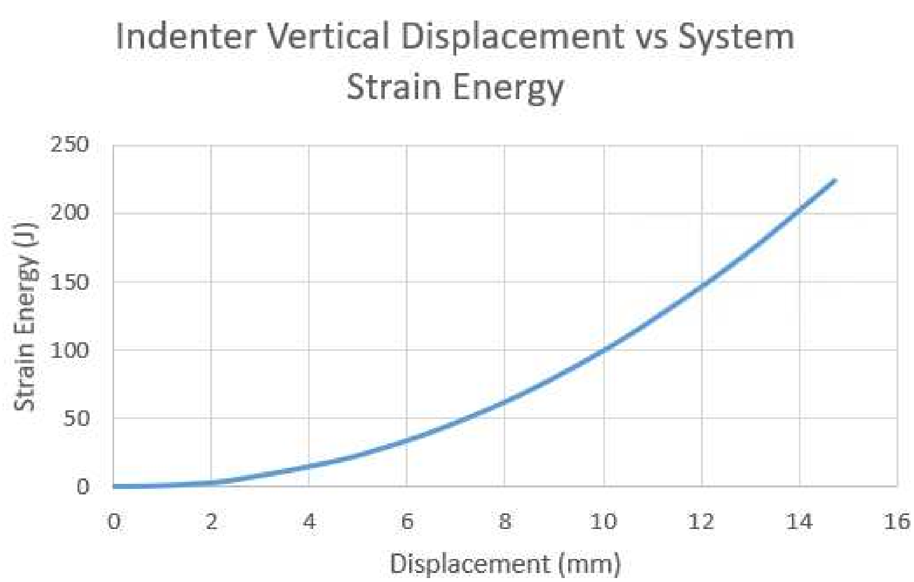

Figure 41 Indentation vs System Strain Energy

4.3.1 Cracks on Top Facer of the Cover Board (CBTF)

Figure 25 (C7) shows that the cracks on the top facer of the cover-board are circular in shape. This can be related to the shear stress distribution of the top facer in the simulation as shown in Figure 42.

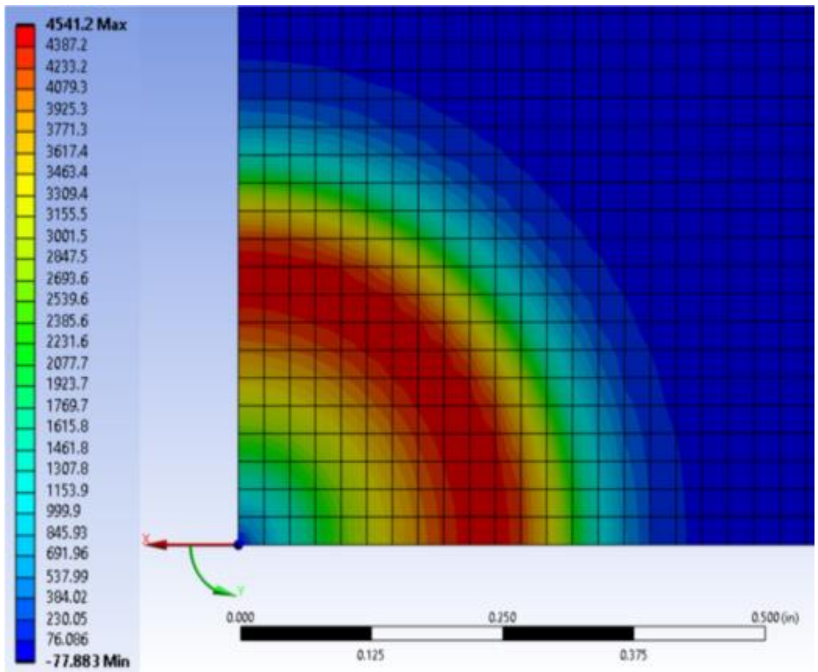

Figure 42 Top view of $\tau_{rz}(psi)$ on top facer of cover board at $E_i = 60.40\ ft \cdot lbf$

4.3.2 Cracks inside the Gypsum Core of Coverboard

The Hertzian cone cracks were observed in the gypsum core after the impact tests. In Figure 28, the axisymmetric nature of the conical crack is very conspicuous. Comparison with FEA simulations shows that near the top surface of the gypsum layer, underneath the indentation area of the gypsum core, the material is subjected to multiaxial compression. Figure 43 shows contours of the τ_{rz} shear stress component in the cylindrical coordinate. These high shear stresses correlate well with the observed cone cracks observed in the gypsum layers. This correlation is not surprising, since the failure of gypsum is expected to be similar to other geomaterials, e.g., rocks and soils where inelastic deformation occurs by frictional sliding over the critical plane of shearing [41] [42]. Since the frictional shear stress depends on the pressure acting over the plane of shearing, the failure criterion should depend on both the normal and the shear stresses. Under these circumstances, the appropriate failure criteria would be the Coulomb-Mohr Failure criterion [43].

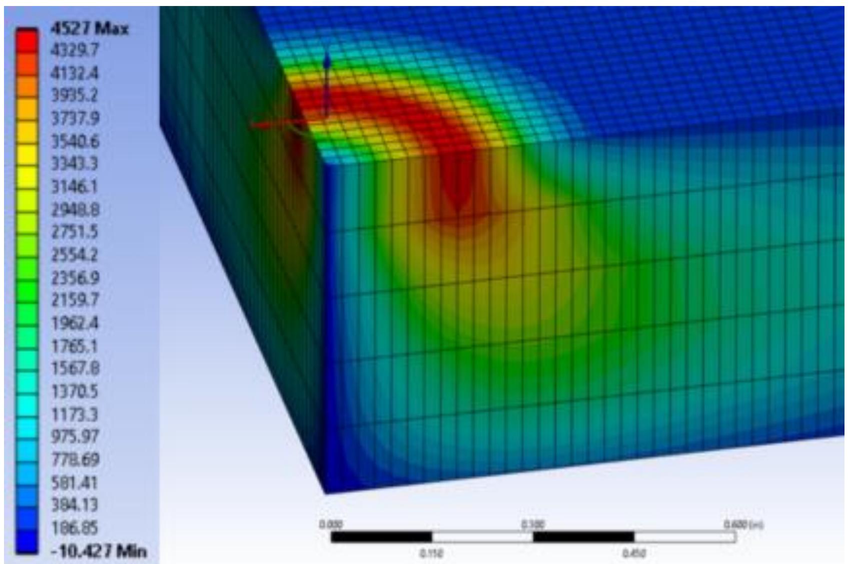

Figure 43 τ_{rz} (psi) inside the gypsum core of cover board

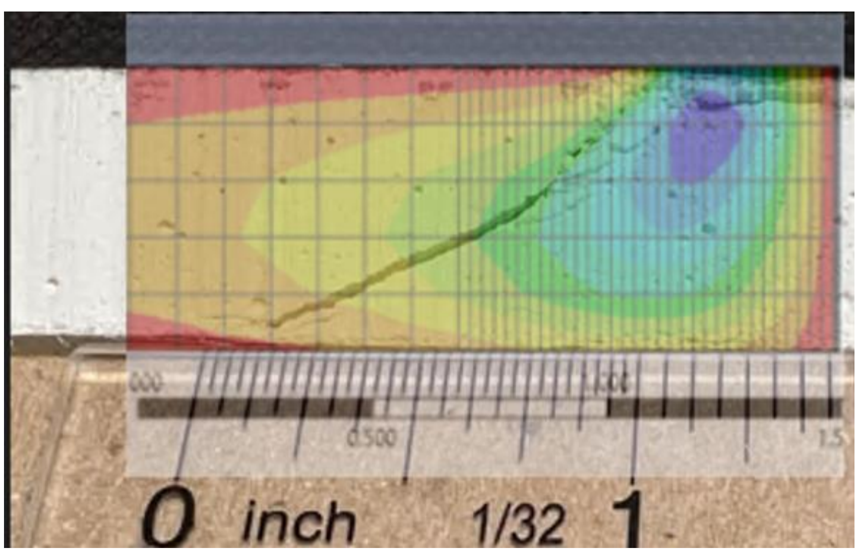

Figure 44 Impact test result vs Simulation result of τ_{rz}

4.3.3 Cracks on Bottom Facer of Coverboard and Top Facer of the Polyiso Board

In the roofing system, the two facer sheets are bonded together by adhesives. Cracks developed on them were nearly identical: they were initiated at the same location—the impact center, and have very similar patterns—radial cracks (Figure 24). For fully-adhered samples, it is difficult to separate the two facer sheets for damage assessment without causing further damage, but with non-adhered samples, the similarity of the cracks on the two facer sheets becomes obvious. The FE simulation also shows that the location on the two facers with the highest principal stresses is directly underneath the impact center (Figure 45), further suggesting that the cracks are likely to be initiated in the center of impact, then develop in radial directions. Unlike those on the top facer of the cover-board, the normal stresses on these two facer sheets along the x and y directions are positive. These two facers crack due to tension.

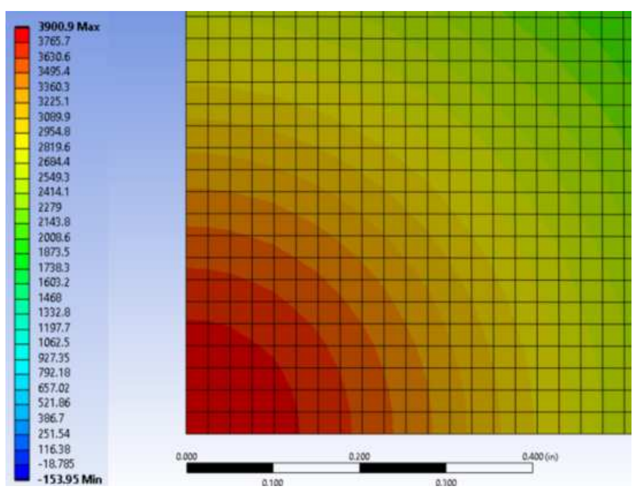

Figure 45 σ_1 (psi) on the bottom facer of the cover board at $E_i = 22.50 ft \cdot lbf$

With increasing impact energy, the increased equivalent indenter displacement increases the tensile stresses on the bottom of the cover board. As shown in the circled zone depicted in Figure 27 and Figure 28. Smaller cracks form near the bottom surface of the gypsum layer developed in a direction perpendicular to this local tension. Fig. 14, shows a contour plot of the maximum principal stresses on the bottom surface of the gypsum layer. The biaxial tension at this location matches the observed cracks shown in Fig. 7 at the more advanced depth of penetration.

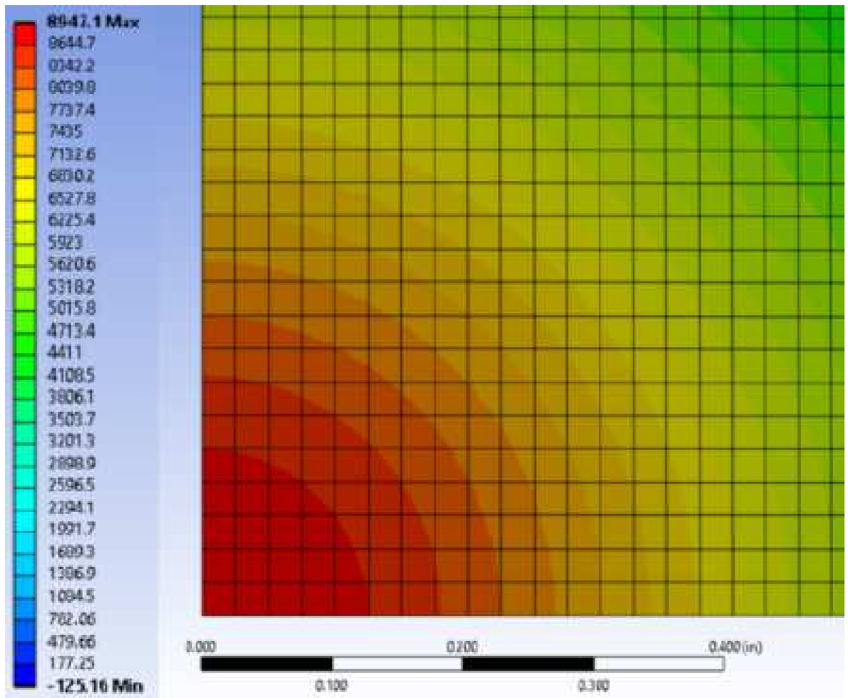

Figure 46 σ_1 (psi) on the bottom surface of the gypsum core at $E_i = 24.31 ft \cdot lbf$

Chapter 5 Simulation on the Effect of Indenter Stiffness

Since steel impactors were expected to behave differently from hailstones during impact events, it was necessary to investigate the effect of indenter stiffness on the distribution of strain energy between the roofing system and the impactors. To this end, a series of finite element simulations was conducted using impactors with varying elastic moduli.

To facilitate the simulation efficiency, the finite element model was simplified to a two-dimensional axisymmetric representation. The quasi-static indentation process was simulated using the material properties listed in was controlled by applying uniform vertical displacement steps throughout all simulations.

Table 12. All indenter and the roofing system were modeled with identical geometric dimensions. The indentation process was controlled by applying uniform vertical displacement steps throughout all simulations.

Table 12 Elastic Material Properties

	Young's Modulus (ksi)	Poisson's Ratio
Steel	29007.5	0.3
	10152.6	0.22
	4641.2	0.3
"Ice"	1348.9	0.325
"POM"	290.1	0.35
	145.0	0.3
"Polymer"	29.0	0.48

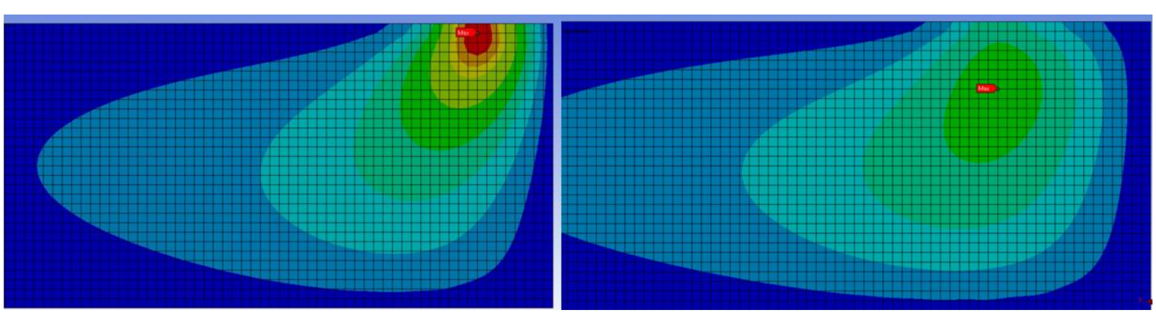

Figure 47

Figure 47 shows the distribution of shear stress τ_{rz} (psi) developed in the gypsum core of the coverboard under steel and ice ball indenters. The shear stress was considerably lower in the case of the ice ball. It was observed that as the indenter stiffness increased, the maximum shear stress in the gypsum layer also increased for the same indentation depth.

With respect to the elastic strain energy distribution between the roofing system and the indenter, the percentage of strain energy carried by the indenter decreased as the indentation depth increased. Across different materials, less stiff indenters absorbed significantly more strain energy. Table 13 ompares the results for steel and ice indenters. At the same indentation depth, the models reported similar total strain energy in the system; however, only about 1% of this energy was carried by the steel indenter, while the ice ball carried 19.7%.

These findings suggest that a steel indenter — and by extension, the steel impactors commonly used in roofing industry impact tests — will impose greater deformation on the roofing system than an ice impactor would under the same impact energy.

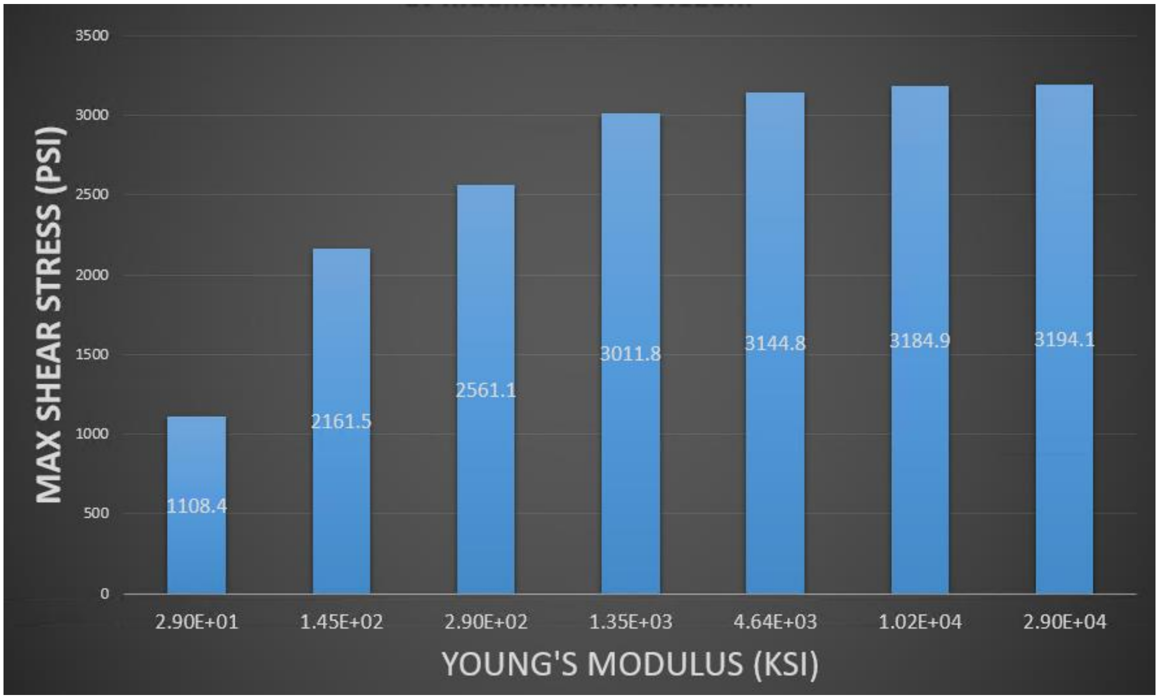

Figure 48 Maximum shear stress τ_{rz} in gypsum core at indentation of 0.128in

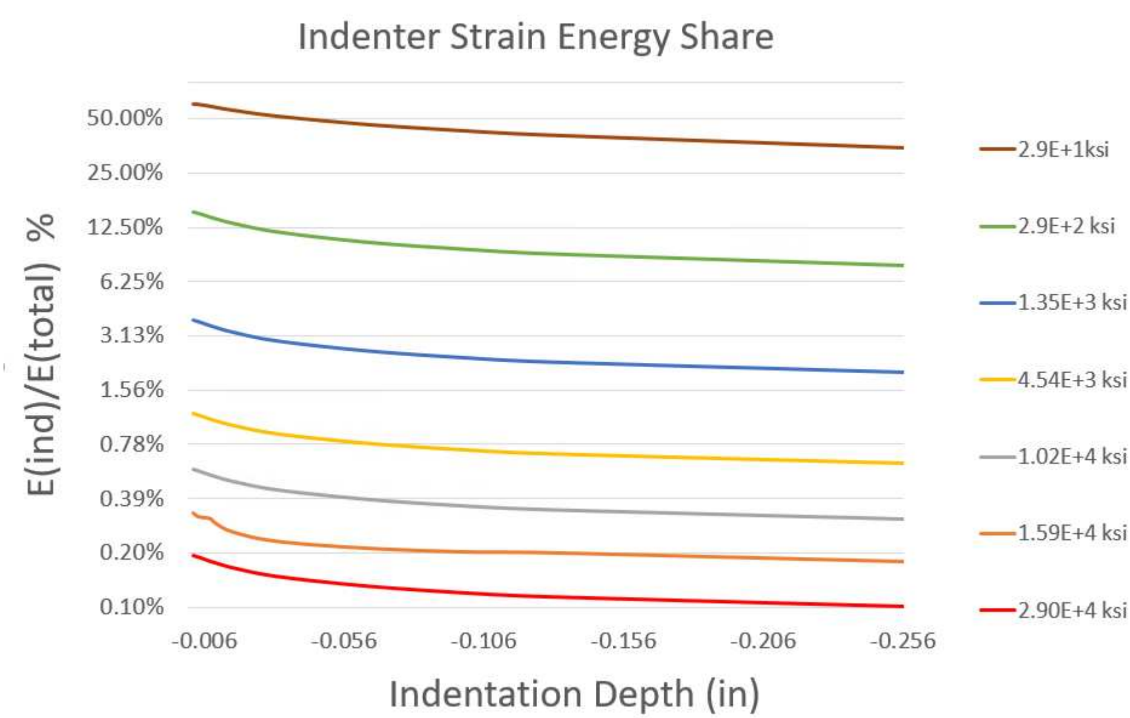

Figure 49 Indenter strain energy share

Table 13 Total Strain Energy of Steel and Ice Indentation

Indentation depth	2.9E+4 ksi ($ft \cdot lbf$)	1.35E+3 ksi ($ft \cdot lbf$)
-0.004	0.001696	0.0016963
-0.008	0.01032	0.009588
-0.016	0.05605	0.054579
-0.032	0.28764	0.28027
-0.064	1.37924	1.34973
-0.128	6.601181	6.46104

Chapter 6

Conclusion

In this study, impact tests of a fully-adhered TPO roofing system utilizing a spherical steel impactor and a cylindrical steel impactor with a spherical head were carried out on the field of the roofing samples, both adhered and non-adhered, to simulate hail impact events. Tests with the spherical impactor covered an impact energy range of $7.80 \sim 15.72\ ft \cdot lbf$, and that of the cylindrical impactor was $22.5 \sim 60.4\ ft \cdot lbf$, which covered the levels of impact energy seen in the FM 4470 testing standard.

Observations of the impact tests were compared with results of Finite element analyses to evaluated the formation mechanisms. Under the testing conditions, the faced gypsum cover board suffered classic Hertzian cone cracks in its core that were closely related to τ_{rz}. Its top facer showed circular cracks caused also by a shear stress member, and its bottom facer was cracked along the radial direction by the bending effect. The Polyiso insulation board were only seen cracked on its top facer and in the foam under the most severe impacts.

The gypsum cover board, specifically, its gypsum core layer, was identified to be the most vulnerable component of the system. It can be cracked by mild hail impact events even at the lowest impact energy level ($7.8\ ft \cdot lbf$) tested, while the surface of the cover board remained undamaged. The top facer of cover board facers was only seen failed at $E_i = 60.4\ ft \cdot lbf$. The damage caused to this top facer was done by a rigid steel impactor, which is very capable of transferring the impact energy into the roofing system, and would not shatter like a hailstone will, especially with that much of impact energy. Thus, the ability of this relatively thick cover board to prevent the TPO roofing system from experiencing functional failure was proved.

A custom impact testing apparatus was also designed and assembled. Its effectiveness on executing the outlined impact test was demonstrated in this research. It's cost-efficient and can be operated by a single person. It provides a practical solution for research institutes and industry members to carry out customized impact tests of various types.

Bibliography

[1] B. A. Baskaran, R. M. Paroli and P. Kalinger, "Advancements and changes in the North American commercial roofing industry," in *International Conference on Building Envelope Systems and Technology*, Bath, 2007.

[2] Maximize Market Research, "Commercial Roofing Market: Industry Analysis and Forecast (2024-2030)," Maximize Market Research, Pune, India, 2024.

[3] Stratview Research, "US Single-Ply Membrane Market Size, Share, Trends, Dynamics, Forecast & Growth Analysis: 2024-2030," Stratview Research, Detroit, MI, USA, 2025.

[4] Atlanta Commercial Roofing, "TPO Roofing: Cost, Material, Repair & Installation Guide," Atlanta Commercial Roofing Contractors, 2024. [Online]. Available: https://atlantacommercialroofingcontractors.com/tpo-roofing-cost-material-repair-installation-guide/. [Accessed March 2025].

[5] AAA Roofing, "Built-Up RooAAA Roofingf vs Modified Bitumen: Contrast of Pros, Cons, & Costs," AAA Roofing, 2025. [Online]. Available: https://www.aaarfg.com/roofing/built-up-roof-vs-modified-bitumen/. [Accessed March 2025].

[6] NJ Metal Roofing, "The Advantages of Metal Roofing for Commercial Buildings," NJ Metal Roofing, 11 September 2023. [Online]. Available: https://nj-metal-roofing.com/commercial-metal-roofing-nj/. [Accessed March 2025].

[7] Overhead Construction & Roofing, "Commercial Spray Foam Insulation," Overhead Construction & Roofing, 2022. [Online]. Available: https://www.overheadconstruction.com/commercial-spray-foam-insulation-roofs/. [Accessed March 2025].

[8] G. Thakre, V. Kaushal and M. Najafi, "A Comparative Impact Assessment of Hail Damage to," *CivilEng,* vol. 6, no. 1, p. 6, 2025.

[9] CIB Working Commission WO83, "TPO Roof membrane systems: A world historical perspective and summary of best practice," International Council for Research and Innovation in Building and Construction, Delft, 2021.

[10] GAF Materials LLC, "Saputo Cheesa USA Facility: Protecting cheese and (computer) chips from Wisconsin weather," GAF Materials LLC. [Online]. [Accessed August 2025].

[11] J. T. Allen and M. K. Tippett, "The characteristics of United States hail reports: 1955–2014," *E-Journal of Severe Storms Meteorology,* vol. 10, no. 3, pp. 1-31, 2015.

[12] National Oceanic and Atmospheric Administration and Storm Prediction Center, "Final Severe Weather Report Database," National Oceanic and Atmospheric Administration (NOAA). [Online]. [Accessed June 2025].

[13] NOAA, "Severe Weather 101 - Hail," National Oceanic and Atmospheric Administration, [Online]. Available: https://www.nssl.noaa.gov/education/svrwx101/hail/. [Accessed May 2025].

[14] FM Approvals, "FM Property Loss Prevention Data Sheets (DS 1-34 Hail Damage)," FM Approvals, 2018.

[15] C. Dieling, M. Smith and M. Beruvides, "Review of Impact Factors of the Velocity of Large Hailstones for Laboratory Hail Impact Testing Consideration," *Geosciences,* vol. 10, no. 12, p. 500, 2020.

[16] National Oceanic and Atmospheric Administration, "Record Setting Hail Event in Vivian, South Dakota on July 23, 2010," National Oceanic and Atmospheric Administration, 23 July 2010. [Online]. Available: https://www.weather.gov/abr/vivianhailstone. [Accessed March 2025].

[17] National Oceanic and Atmospheric Administration, "Storm Prediction Center: 2022 Annual Final Report Summary," National Oceanic and Atmospheric Administration, [Online]. Available: https://www.spc.noaa.gov/climo/summary/. [Accessed January 2024].

[18] B. K. Sullivan, "Nobody Seems to Know Why Hail Storm Losses Suddenly Began Rising in 2008," Insurance Journal, 17 June 2019. [Online]. Available: https://www.insurancejournal.com/news/national/2019/06/17/529518.htm. [Accessed January 2024].

[19] M. S. Slocumb, "Approval Report: fastorchSBS FT120GSA, FT160CSA BASE PLIES AND fireguardfastorchSBS FGFT160CWH, FGFT160GWH CAP SHEETS TORCHED OVER A GYPSUM COVER BOARD IN CLASS 1 ROOF DECK ASSEMBLIES," FM Approvals, Norwood, MA, 2007.

[20] V. A. Crenshaw, "Major Building Code Requirements For Impact Resistance of Low-Slope Roofing Systems: A Review and Comparison of Test Procedures," The Roof Consultants Institute, Raleigh, NC, 2008.

[21] D. E. Brotherson, "Investigation to Identify Performance Criteria and Test Methods for Evaluating Single-Ply Roofing Systems," U.S. Army Corps of Engineers, Construction Engineering Research Laboratory, Champaign, IL, 1987.

[22] M. S. Graham, "Understanding FM VSH," *Professional Roofing,* Dec 2017.

[23] FM Approval, "Examination Standard for Single-Ply, Polymer-Modified Bitumen Sheet, Built-Up Roof (BUR) and Liquid Applied Roof Assemblies for Use in Class 1 and Noncombustible Roof Deck Construction," FM Approval, 2022.

[24] FM Approval and ANSI, "American National Standard for Impact Resistance Testing of Rigid Roofing Materials by Impacting with Freezer Ice Balls," FM Approval; ANSI;, 2020.

[25] ANSI and FM Approvals, "American National Standard for Impact Resistance Testing of Rigid Roofing Materials by Impacting with Freezer Ice Balls," ANSI; FM Approvals, 2020.

[26] UL Standards & Engagement, "ANSI/UL 2218A Standard for Impact Resistance of Roofing Systems," UL Standards & Engagement, Northbrook, IL, 2024.

[27] McMaster-Carr, "T-Slotted Framing: Single Four Slot Rail, Silver, 1.5" High x 1.5" Wide, Solid," McMaster-Carr. [Online]. [Accessed March 2025].

[28] McMaster-Carr, "T-Slotted Framing: Heavy Duty Rail Slide for 40mm and 1.5" High Single Rail," McMaster-Carr. [Online]. [Accessed March 2025].

[29] McMaster-Carr, "T-Slotted Framing: Rail Slide with Cam Handle for 1.5" and 40mm High Rail," McMaster-Carr, [Online]. Available: https://www.mcmaster.com/5537T434/. [Accessed March 2025].

[30] Y. Ding, H. F. Nied, S. Hung and R. Nagarajan, "Assessment of Impact Damage in Fully Adhered Commercial Roofing Systems," in *SPE ANTEC*, St. Louis, 2024.

[31] GAF, "EverGuard TPO Membrane," GAF, 2024.

[32] Y. Ding, "Performance Evaluation of Washer Plates in Thermoplastic Polyolefin Roofing Assemblies Subjected to Wind-Induced Uplift," Lehigh University, Bethlehem, PA, 2025.

[33] GAF, "DensDeck® StormX™ Prime Roof Board," [Online]. Available: https://www.gaf.com/en-us/roofing-materials/commercial-roofing-materials/cover-boards/densdeck-stormx-prime-roof-board.

[34] T. Luo, H. F. Nied, L.-Y. Yang and S. Bhawalkar, "Impact Modeling of Single-ply TPO Roofing Systems," in *SPE ANTEC 2016*, Indianapolis, Indiana, USA, 2016.

[35] D. A. Boardman and D. E. Brown, "Developing a Test Method for a Very Severe Hail Rating for Low Slope Roofing Assemblies," in *Roofing Research and Standards Development: 8th Volume*, West Conshohocken, ASTM International, 2015, pp. 1-13.

[36] S. Bhawalkar, T. Yang and T. J. Taylor, "Understanding the Puncture Resistance of Thermoplastic Polyolefin Membranes," in *Roofing Research and Standards Development: 8th Volume*, West Conshohocken, PA, ASTM International, 2015, pp. 14-29.

[37] H. Hertz, "The contact of elastic solids," *Journal für die reine und angewandte Mathematik,* vol. 92, pp. 156-171, 1881.

[38] C. Kocer and R. E. Collins, "Angle of Hertzian cone cracks," *Journal of the American Ceramic Society,* vol. 81, no. 7, pp. 1736-1742, 1998.

[39] C. Kocer, "Using the Hertzian fracture system to measure crack growth data: A review," *International Journal of Fracture,* vol. 121, pp. 111-132, 2003.

[40] ANSYS Inc., "ANSYS Mechanical Help," ANSYS Inc..

[41] N. Brantut, A. Schubnel and Y. Guéguen, "Damage and rupture dynamics at the brittle-ductile transition: The case of gypsum," *Journal of Geophysical Research: Solid Earth,* vol. 116, no. B1, 2011.

[42] J. Xu, X. Xiao, X. Lv, P. Guo and Y. Peng, "Simulation of compression-induced shear-mode cracks in rocks based on experimental investigations performed on gypsum specimens," *Bulletin of Engineering Geology and the Environment,* vol. 79, pp. 4309-4319, 2020.

[43] J. Handin, "On the Coulomb-Mohr failure criterion," *Journal of Geophysical Research,* vol. 74, no. 22, pp. 5343-5348, 1969.

[44] F. Findik, "Polymeric materials and their applications," *Sustainable Engineering and Innovation,* vol. 7, no. 1, pp. 15-40, 2025.

[45] D. LeComte, "U.S. Weather highlights 2024: Five Gulf Hurricanes, Tornado Outbreaks, Historic Heat Wave," *Weatherwise,* vol. 78, no. 2, pp. 26-35, 2025.

[46] ANSI and FM Approvals, "American National Standard for Evaluating the Simulated Wind Uplift Resistance of Roof Assemblies Using Static Positive and/or Negative Differential Pressures," ANSI, FM Approvals, 2020.

[47] J. Payne, H. F. Nied and L.-Y. T. Yang, "Modeling of Single-ply Thermoplastic Polyolefin Roofing," in *SPE ANTEC 2013*, Cincinnati, Ohio, USA, 2013.

[48] National Centers for Environmental Information, "Climate Extremes Index (CEI)," National Oceanic and Atmospheric Administration (NOAA), n.d.. [Online]. Available: https://www.ncei.noaa.gov/access/monitoring/cei/graph. [Accessed 5 March 2025].

[49] Zion Market Research, "Commercial Roofing Market - By Product Type, Application, and Region - Global Industry Perspective, Comprehensive Analysis and Forecast, 2023-2032," Zion Market Research, New York, 2025.

[50] Dassault Systèmes, "SOLIDWORKS Help," Dassault Systèmes.

[51] FM Approval, "Examination Standard for Single-Ply, Polymer-Modified Bitumen Sheet, Build-Up Roof (BUR) and Liquid Applied Roof Assemblies for Use in Class 1 and Moncombustible Roof Deck Construction," Fm Approval.

[52] K. Westover, "Defending Against Very Severe Hail," GAF, 30 January 2023. [Online]. Available: https://www.gaf.com/en-us/blog/building-science/defending-against-very-severe-hail-281474980224963. [Accessed March 2025].

[53] W. Li, "Adhesive Applied Roofing System (Master's Thesis)," Department of Civil Engineering, University of Ottawa, Ottawa, Ontario, Canada, 2010.

[54] J. T. Allen, I. M. Giammanco, M. R. Kumjian, H. J. Punge, Q. Zhang, P. Groenemeijer, M. Kunz and K. Ortega, "Understanding Hail in the Earth System," *Reviews of Geophysics,* vol. 58, no. 1, pp. n/a-n/a, 2020.

[55] FM Global, "FM Property Loss Prevention Data Sheets," FM Global, Johnston, RI, 2025.

Appendix A

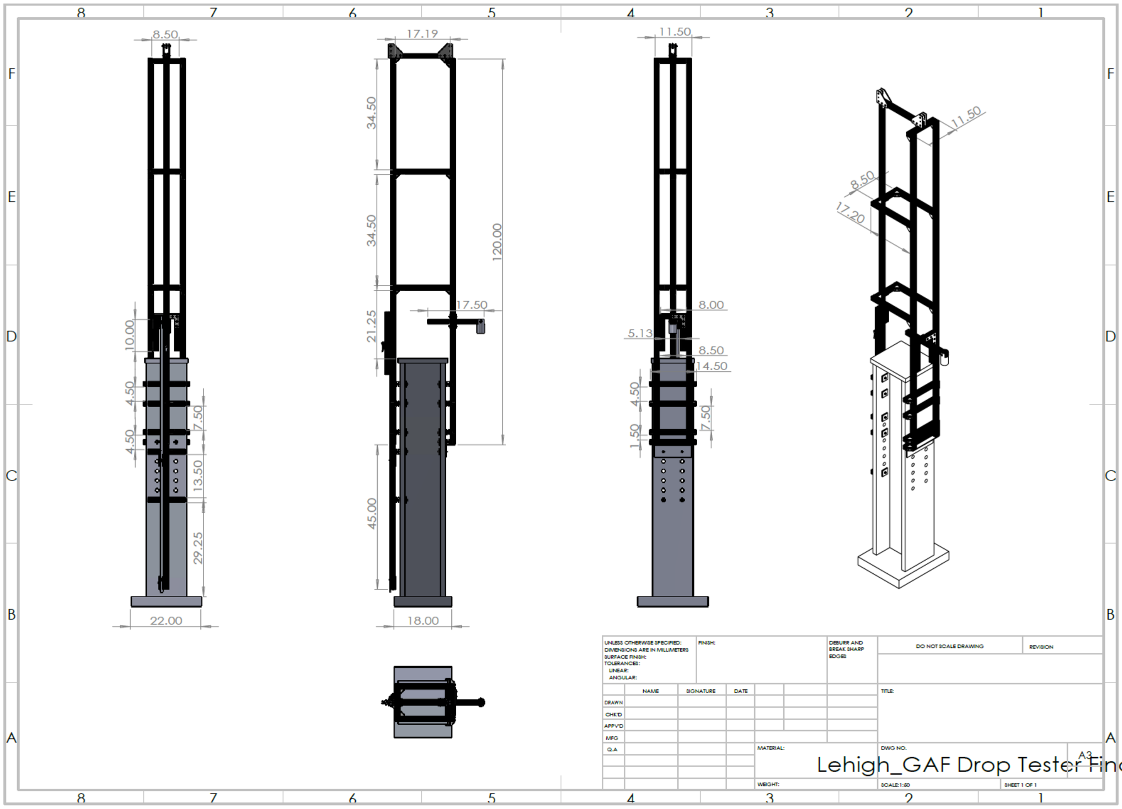

8.50
17.19
11.50
34.50
34.50
120.00
21.25
17.50
8.00
5.13
8.50
14.50
10.00
4.50
4.50
7.50
13.50
29.25
45.00
4.50
1.50
7.50
22.00
18.00
11.50
8.50
17.20
Lehigh_GAF Drop Tester

VITA

Yi Ding was born in Changchun, China, in 1987. He received the Bachelor of Engineering degree in Electrical Automation from the University of Science and Technology Beijing (USTB), China, in 2010. He later earned the Master of Engineering degree in Mechanical Engineering from Illinois Institute of Technology in Chicago, United States, in 2015.

He is currently pursuing both the Master of Science and Doctor of Philosophy degrees in Mechanical Engineering at Lehigh University. His research focuses on solid mechanics and finite element simulation, particularly in the context of TPO commercial roofing systems.